SELEN YILMAZ

ATILIM UNIVERSITY 2023

A STUDY ON MICROSTRIP ANTENNA DESIGN FOR 77 GHZ RADAR SYSTEMS

THE GRADUATE SCHOOL OF NATURAL AND APPLIED SCIENCES
OF
ATILIM UNIVERSITY

SELEN YILMAZ

A MASTER OF SCIENCE THESIS
IN
THE DEPARTMENT OF ELECTRICAL AND ELECTRONICS ENGINEERING

JANUARY 2023

A STUDY ON MICROSTRIP ANTENNA DESIGN FOR 77 GHZ RADAR SYSTEMS

A THESIS SUBMITTED TO
THE GRADUATE SCHOOL OF NATURAL AND APPLIED SCIENCES
OF
ATILIM UNIVERSITY

BY

SELEN YILMAZ

IN PARTIAL FULFILLMENT OF THE REQUIREMENTS
FOR
THE DEGREE OF MASTER OF SCIENCE
IN
ELECTRICAL AND ELECTRONICS ENGINEERING

JANUARY 2023

Approval of the Graduate School of Natural and Applied Sciences, Atılım University.

Prof. Dr. Ender Keskinkılıç
Director

I certify that this thesis satisfies all the requirements as a thesis for the degree of **Master of Science in Electrical and Electronics Engineering Department, Atılım University**.

Prof. Dr. Reşat Özgür Doruk
Head of Department

This is to certify that we have read the thesis A STUDY ON MICROSTRIP ANTENNA DESIGN FOR 77 GHZ RADAR SYSTEMS submitted by Selen Yılmaz and that in our opinion it is fully adequate, in scope and quality, as a thesis for the degree of MASTER OF SCIENCE.

Prof. Dr. Ali Kara
Co-Supervisor

Asst. Prof. Dr. Yaser Dalveren
Supervisor

Examining Committee Members:

Assoc. Prof. Dr. Hüseyin Uğur Yıldız
Electrical and Electronics Engineering Department,
TED University

Asst. Prof. Dr. Yaser Dalveren
Electrical and Electronics Engineering Department,
Atılım University

Prof. Dr. Reşat Özgür Doruk
Electrical and Electronics Engineering Department,
Atılım University

Date: 12.01.2023

I declare and guarantee that all data, knowledge, and information in this document has been obtained, processed, and presented in accordance with academic rules and ethical conduct. Based on these rules and conduct, I have fully cited and referenced all material and results that are not original to this work.

Name, Last Name: SELEN YILMAZ

Signature:

ABSTRACT

A STUDY ON MICROSTRIP ANTENNA DESIGN FOR 77 GHZ RADAR SYSTEMS

Yılmaz, Selen

M.S., Department of Electrical and Electronics Engineering

Supervisor: Asst. Prof. Dr. Yaser Dalveren

Co-Supervisor: Prof. Dr. Ali Kara

January 2023, 59 pages

This thesis presents a comprehensive investigation into the design and operational behavior of series-fed microstrip patch antenna array for the 77 GHz automotive radar. Initially, the theoretical background information on the theory of microstrip antenna, patch antenna array, frequency scanning array and Chebyshev array are provided. A full-wave finite element method-based simulation tool is used to design and slightly tune the dimensions of the antennas as a parametric study. At the first stage, a series fed linear Chebyshev patch array with resonance at 76.5 GHz is designed representing one transmit channel of the antenna. Shorting pins are loaded to transition structure of ground-signal-ground (GSG) padding to enhance the total gain. Comparative analysis between vialess and via loaded cases is conducted in terms of bandwidth and gain. At the last stage, 76.5 GHz linear patch antenna array is converted into a 79 GHz linear patch antenna array by optimizing the GSG padding dimensions, scaling the spacings between each two adjacent array elements and the length of array elements. Two designs are proposed to assess the effect of scaling method at this stage. Comparative analysis in terms of the beam steering angle, the impedance bandwidth, the overall gain and the sidelobe level suppression is conducted between these two designs.

Keywords: Dolph-Chebyshev Distribution, Frequency Scanning Array, Linear Array, mmWave, Patch Array Antenna.

ÖZ

77 GHZ RADAR SİSTEMLERİ İÇİN MİKROŞERİT ANTEN TASARIMI VE ANALİZİ

Yılmaz, Selen
Yüksek Lisans, Elektrik ve Elektronik Mühendisliği Bölümü
Tez Yöneticisi: Asst. Prof. Dr. Yaser Dalveren
Ortak Tez Yöneticisi: Prof. Dr. Ali Kara

Ocak 2023, 59 sayfa

Bu tez, 77 GHz otomobil radarı için seri beslemeli mikroşerit yama dizi antenin tasarımı ve operasyonel davranışına yönelik kapsamlı araştırmasını takdim etmektedir. Öncelikli olarak, mikroşerit anten, yama dizi anten, frekans taramalı dizi anten ve Chebyshev dizi anten teorisi hakkında teorik altyapı bilgisi temin edilmiştir. Antenleri tasarlamak ve boyutlarını hassas bir şekilde ayarlamak için sonlu eleman metoduna dayalı tam dalga simülasyon aracı kullanılmıştır. İlk aşamada, 76.5 GHz rezonans frekansında çalışan seri beslemeli doğrusal Chebyshev dizi anten bir verici kanalını temsil etmesi üzerine tasarlanmıştır. Kazancı geliştirmek için toprak-sinyal-toprak geçiş yapısında kullanılmak üzere kısa devre pinlerinden yararlanılmıştır. Pinsiz ve pinli tasarımların bant genişliği ve kazanç bakımından karşılaştırmalı analizi yapılmıştır. Son aşamada, 76.5 GHz doğrusal dizi yama anten 79 GHz doğrusal dizi yama antene GSG geçiş yapısı boyutları optimize edilerek ve her bitişik iki yama elemanı arasındaki aralıklandırma ve yama elemanı uzunlukları ölçeklenerek dönüştürülmüştür. Ölçeklendirme yönteminin etkisini değerlendirebilmek adına bu aşamada iki tasarım sunulmuştur. Bu iki dizi yama anten tasarımının operasyonel özelliklerinin ana kulak yönlendirilme açısı, empedans bant genişliği, total kazanç ve yan kulak baskılanması bakımından karşılaştırmalı analizi yapılmıştır.

Anahtar Kelimeler: Doğrusal Dizi, Dolph-Chebyshev Dağılımı, Frekans Taramalı Dizi, Milimetre Dalga, Yama Dizi Anten.

To My Grandfather

ACKNOWLEDGEMENTS

First, I would like to express my sincere and eternal gratitude to my advisors Assoc. Prof. Dr. Yaser Dalveren and Prof. Dr. Ali Kara for their continuous support and patience. Their guidance led me to the right path throughout all my thesis and my entire master's study as well. It has been such a great honor and privilege for me to study under the supervision of Assoc. Prof. Dr. Yaser Dalveren and Prof. Dr. Ali Kara.

I would like to express my appreciation to Assoc. Prof. Dr. Yaser Dalveren especially because as being my thesis supervisor creating the opportunity for me to conduct research in the field of antenna, and his encouraging attitude. With his invaluable mentoring, constructive advice, and everlastingly positive approach, he truly is a distinguished scientist and teacher.

I would like to express my deepest thanks to Prof. Dr. Ali Kara for his continuous motivating positive attitude, insightful contributions, and his unique precious guidance throughout all my master's study. It has been such a great chance for me to be his student.

I would like to express my eternal gratitude to Prof. Dr. Reşat Özgür Doruk for providing me the opportunity to access his computer for the simulations, his positive encouraging attitude and for his wise contributions during my thesis defense presentation session.

I would like to thank the chairman of my thesis committee Assoc. Prof. Dr. Hüseyin Uğur Yıldız for his insightful comments and encouragement, but also for the challenging question which incented me to widen my research from various perspectives.

TABLE OF CONTENTS

LIST OF TABLES

TABLES

LIST OF FIGURES

FIGURES

LIST OF SYMBOLS

λ_0	:	Free-Space Wavelength
λ_g	:	Guided Wavelength
ε_r	:	Relative Dielectric Constant
ε_{reff}	:	Effective Dielectric Constant
tan δ	:	Loss Tangent of Dielectric Substrate Material
$\|\Gamma\|$	:	Reflection Coefficient
VSWR	:	Voltage Standing Wave Ratio
f_r	:	Resonance Frequency
SLL	:	Side Lobe Level
HPBW	:	Half Power Beamwidth
GSG	:	Ground-Signal-Ground
h	:	Substrate Thickness
W	:	Width of Patch
ΔL	:	Extended Incremental Length of Patch
L	:	Actual Length of Patch
L_e	:	Effective Length of Patch
Θ_s	:	Beam Steering Angle
$\Delta\varphi$	:	Phase Shift Between Two Successive Radiating Elements

d	:	Distance Between Two Successive Radiating Elements
G	:	Gain
BW	:	Impedance Bandwidth
D	:	Directivity
N	:	Number of Radiating Patch Elements
Z_0	:	Characteristic Impedance
RL	:	Return Loss
U_{max}	:	Maximum Radiation Intensity
Q_t	:	Total Quality Factor
FEM	:	Finite Element Method
HFSS	:	High Frequency Structure Simulator
mmWave	:	Millimeter-Wave Band
MPA	:	Microstrip Patch Antenna
Via	:	Vertical interconnect access (vertical electrical connection)
V2V	:	Via to via

CHAPTER 1

INTRODUCTION

With worldwide revolutionary changes in the radio communications field, antennas have received considerable attention over the years. An antenna is essential to radiate and receive the electromagnetic energy in any broadcast or wireless radio communication system and therefore their performance is significant to the operation of the complete radio system. Microstrip antennas are one of the most widely preferred type of antenna from among numerous types of antennas. Hence, they are employed in a broad range of fields from missile systems to autonomous vehicle applications. Their low profile, small volume, low mass, low cost, conformability to planar and nonplanar surfaces, simple structure to manufacture via photolithography, ease of installation, ease of integration with other microwave circuitries, cost-effectiveness, and simplicity for mass production due to their layered compact structure cause them to be highly favorable [1]. Furthermore, they are versatile regarding the resonance frequency, radiation pattern, polarization and impedance matching in case of selecting the compatible patch shape and excitation mode. However, microstrip antennas still have some operational drawbacks in terms of efficiency, polarization purity, RF power handling capability, spurious radiation due to their imperfect feed transition structure and narrow bandwidth, restricting their areas of use [1]. It is known that some fundamental methods have been developed in the recent decades to enhance the impedance bandwidth and total gain, such as use of a low dielectric constant thick substrate [1-3], use of square/rectangular/circular shaped patch elements [4-7], incorporating single or multi-slots to the radiating patch [8,9], implanting of shorting pin(s) or shorting wall(s) for providing capacitive coupling [10,11], use of defected ground plane structures [12-14], use of linear array of microstrip patches [15-20], substrate integrated waveguide technique [21,22], and stacked patch configurations [23,24]. Within these optimizations, when the proper patch configuration is designed, building up an array is proven to be one of the most effective methods of enhancing the directivity, and synthesizing a particular radiation pattern, which cannot be

achieved with a single element. Moreover, arrays provide angular beam scanning feature by varying the operating frequency [25].

Emphasis on automotive safety has been gradually improving by the automakers to ensure a safer and more comfortable travel to the occupant(s) of the vehicle. Therefore, antennas with wide bandwidth and with certain radiation pattern characteristics has been a commonly sought-after topic for the last two decades to be utilized in the various applications in automotive radar industry. Several active advanced driver-assistance (ADAS) systems such as LiDAR, infrared camera and ultrasonic sensors, and radar have been developed to provide applications like adaptive cruise control, blind spot detection, parking aid, obstacle or pedestrian crash avoidance system, forward collision warning system, and driver monitoring system to help improve the driving experience [26]. On the other hand, some of these systems are not capable of operating under the harsh climate conditions thereby making the reliability of these systems controversial. It is shown that radar devices have much less shortcoming than LiDARs or camera sensors since they can work under extreme weather conditions like heavy snow, heavy rain or fog with high accuracy operation performance [26]. Because of that LiDAR works on the principle of bouncing the laser beam off the surrounding obstacles so that it can recognize them, however it can also interfere with raindrops, resulting in the refraction of its beam into an undesired direction and so providing no result [26]. This unfavorable mechanism also occurs when there is fog, dust or heavy snow making LiDAR prone to underperform under certain climate conditions, unlike its other counterparts [26]. Contrarily to LiDAR, a radar is reasonably more robust to adverse weather conditions than the other driver assistive systems as it is proven to be there is little to no effect in the amount of atmospheric attenuation or reflection of its electromagnetic signal energy in 70-80 GHz frequency range [26]. Because radar basically uses microwave that is reflected by certain materials like metal or concrete but is able to go through living beings or obstacles made of plastic [27]. Consequently, radar can be preferred primarily in the making of innovative driver assistance systems to help reduce the number of automobile accidents.

Collision avoidance radar, being one of the most significant sensors of the modern driver assistance system, is used to recognize the range as well as velocity and angle of pedestrian or any kind of obstacle and to notify the driver about it, and it may also

cause the automobile to react to the pedestrian or obstacle by applying the automatic braking system if the driver takes no action [27]. The radar devices are typically divided into three main categories according to the range they cover as short-range (SRR), medium-range (MRR), and long-range (LRR) radar. Figure 1.1. demonstrates diverse types of driver assistance safety applications embedded in various parts of a vehicle.

Figure 1.1: Top view of advanced-driver assistance system radar (ADAS) [26]

Car manufacturers worldwide have been making comprehensive research studies to develop advanced sensors due to the many benefits provided by radars. Since the late ninety's, several radar systems have been assembled at the various parts of an automobile, which serves for different purposes listed below:

- SRR module for lane detection installed in the back corner of the car.
- SRR and MRR module for park assist in rear and/or front bumper of the car.
- MRR for blind spot detection located under the rear bumper and in side mirrors.
- LRR for adaptive cruise control, automatic emergency braking and forward collision warning mounted at the front grill of the vehicle.
- Driver attentiveness monitoring in-car camera-based system equipped with radar sensor that track driver's eye movements and head position to produce a warning in case of detection of the driver's state of drowsiness.

Preliminary investigations on use of radar systems in automobile industry began prior to its implementation in the passenger car as a collision mitigation system in the late seventy's [28]. 24 GHz band and 77 GHz band have been allocated for use in this

domain since then. For 24 GHz band there was two options available for the automobile market, one was narrowband with 200 MHz span from 24.05 GHz to 24.25GHz, and the other was ultra-wide band (UWB) with 5 GHz bandwidth from 21.65 GHz to 26.65 GHz [29]. But, due to the spectrum regulations and standards published by the European Telecommunications Standards Institute (ETSI) and the Federal Communications Commission (FCC), the 24 GHz UWB band was phased out in 2022 for both Europe and the USA [29]. Only the 200 MHz wide narrowband ISM band will be available at 24 GHz [29]. Looking at 77 GHz, there are two allocated frequency ranges for automotive radar, one to be used for long range radar (LRR) in the range 76 to 77 GHz and the other for short range radar (SRR) in the band from 77 to 81 GHz [29]. When the demand for higher range resolution with high directivity narrower beamwidth is considered in emerging automotive radar implementations, 24 GHz automotive radar is highly probable to shift to 77 GHz band. A 77 GHz radar sensor is proven to achieve twenty times higher range resolution, due to its relatively smaller wavelength, when compared to 24 GHz radar, which enables a better separation of objects, for example detecting a person standing near a car, making itself also beneficial for the upcoming era of completely autonomous driving [29]. In addition, the substantial risk of signal interference from other devices operating at 24 GHz band cannot be neglectable because of its allocation to industrial, scientific, and medical (ISM) use and its quite narrow bandwidth [29]. Band allocations are briefly presented in the following figure 1.2 for convenience.

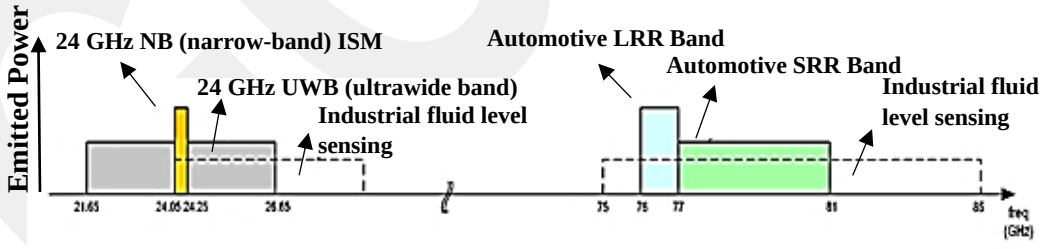

Figure 1.2: 24 GHz and 77 GHz spectrum allocations on a global scale [29]

Studies on 77 GHz antennas have been reported for approximately twenty years [30]. When the idea of building an automotive radar first came out in the seventies, and after the early implementations of radar systems on the bus lines in the USA, the car accident statistics showed 21 percent decrease compared to the previous year [39]. This situation significantly provided an inspiration to many engineers then, thus since that time there has been a substantial improvement in automotive radar antenna design.

One of the initial investigations into 77 GHz antenna was made as an automotive collision avoidance radar antenna consisting of an orthogonally fed square radiating patch on a 150 μm thick silicon substrate, incorporating Schottky diodes to prevent the excessive accumulation of charge on the conducting patch, however it's directivity was poor due to the spurious radiation of mismatched feed transmission lines [43]. The main problem of 77 GHz automobile antenna is insufficient gain, and it is extremely difficult to synthesize a narrow beam with low side lobe levels. Some pyramidal and conical horn antennas coupled with a dielectric lens to improve the gain have been proposed but they have a generous size, and they are bulky to be used in automotive radar chipset [40,41]. It is also shown that multi-layered substrate integrated waveguide cavity-backed patch with stepped waveguide horn was studied as 16x16 array elements to obtain high gain, coming with the expense of its quite complex structure and high manufacture cost [42]. As a result, the general tendency of automotive industry has been towards compact beam focusing and steering microstrip patch antenna arrays rather than conventional bulky horn antennas. Various patch antenna studies as linear or planar phased array configurations have been conducted to enhance the gain, however increasing the number of patch elements hasn't been so effective on its own, utilizing a patch amplitude weighting method when building up a patch array was shown to significantly reduce the sidelobe levels and in far-field it was quite useful to form a specific radiation pattern [15-20]. Therefore, Dolph-Chebyshev distribution has been a common approach to obtain the desired radiation pattern characteristics that has been employed to design a complete transceiver antenna module recently [15-20]. A selection of published studies in this context is summarized in table 1.1.

Table 1.1: Comparison of W-Band Antennas

Type	**Impedance BW (GHz)**	**Gain (dBi)**	**Side-lobe level (dB)**	**Radiation Efficiency (%)**	**Ref.**
Microstrip Patch Array	77-81	12	< -20	-	[31]
Microstrip Planar Array	81-86	14	< -5	90	[32]

Table 1.1 (continued)

SIW Cavity Array	77-86	15	< -11	-	[33]
Rectangular Patch Array	75.04-77.95	16.56	< -17.2	-	[34]
Corporate-Fed Patch Array	69.5-75	7.49	-	56.3	[35]
This Work	75.6-77.6	18	< -16.7	96.8	-

Despite the improvements in 77 GHz antenna across the world for the last two decades, there are a very few studies in this domain currently available in Turkey. A 77 GHz single element patch antenna with uniplanar electromagnetic bandgap structure with 7 dBi gain has been investigated in [36]. Another attempt has been a strip dipole antenna with L and T shaped patches used on the same silicon chip for 77 GHz resonance, but its peak gain is only at 5.33 dBi presented in [37]. A phased 1 x 4 patch array has been developed with a maximum gain of 9.7 dBi by means of Klopfenstein tapering microstrip-to-coplanar waveguide transition is reported in [38]. As a result, when the restricted literature particularly in Turkey and the rapidly growing demand in automotive industry are taken into consideration, there is a significant need for further research effort on 77 GHz antenna.

In this study, an improved compact design is proposed by using a single layered Chebyshev weighted patch array antenna fed via shorting pin incorporated ground-signal-ground (GSG) padding transition structure. This work fundamentally consists of two stages in terms of different operating ranges. As the first stage, the main objective of this study is to obtain 2 GHz wide resonance bandwidth at 76.5 GHz with pencil beam radiation pattern with a gain of above 15 dBi. In accordance with this purpose, 16-element array structure is preferred to obtain high gain and narrow beamwidth and each patch width is tapered by using the distribution method of Chebyshev's polynomial to form the desired low sidelobe level radiation pattern. The significance of GSG padding as a microstrip line to waveguide feed transition structure for mmWave band is discussed in detail. In addition, the effect of loading shorting pins into GSG padding is evaluated in terms of bandwidth and gain enhancement. At the

second stage, the operating bandwidth is aimed to be shifted to 79 GHz without deteriorating its directivity. For this purpose, each spacing between every two adjacent patch elements is decreased by a constant factor and GSG padding dimensions are optimized. Lastly, two different planar arrays for both 76.5 GHz and 79 GHz operation, consisting of three consecutive linear arrays each representing a transmit channel are designed to obtain additional angular information.

In compliance with these objectives, this thesis is organized as follows: the first chapter presents the problem statement, motivation, and the hypothesis as a proposed solution. The second chapter provides theoretical insight into microstrip antenna theory, explaining the basic antenna parameters, and both the theoretical and computational electromagnetics solver methods. In the following chapter, design and simulation procedures are presented comprehensively. Standard procedures for building up a patch array are not always established when working at mmWave band. Therefore, all the steps of a simulation-based design process are presented both for 76.5 GHz and 79 GHz antennas, with a comparative analysis between their performance characteristics and offering possible optimizations that can be applied to enhance the performance of the antennas for future endeavors. In the last chapter, conclusions drawn from the entire study are presented.

CHAPTER 2

MICROSTRIP PATCH ANTENNA THEORY

Microstrip patch antenna (MPA) type is preferred over the other type of antennas for design and simulation process of this study as per the stated reasons in the previous chapter. No antenna can be scientifically designed or analyzed before comprehension of basic antenna parameters, operational principles, feed techniques and methods of analysis. Depending only on the theoretical results or only on a computer aided design tool on its own does not always yield the most accurate result, thus they should always be combined with each other. Therefore, theoretical background of microstrip antenna is discussed in this chapter in the simplest sense possible, and so [1] is taken as reference throughout the whole chapter.

2.1 Fundamental Principles of Microstrip Antenna Operation

A conventional microstrip antenna has a low profile basically consisting of three parts, which are a conducting patch on top to radiate the power in the desired direction, a dielectric substrate in the middle to separate the top and the bottom metal layers to generate electric field, and the bottom conductor ground layer serving as the reference potential plane or a return path for current flowing from the other components of antenna, as shown in Figure 2.1.

Microstrip patch is made from a very thin conducting strip ($t << \lambda_0$), of copper or aluminum foil sheet. The length L of the patch element is in the range of $\lambda_0/3 < L < \lambda_0/2$. Patch is chemically etched on a dielectric layer having a thickness of $0.003\lambda_0 \leq h \leq 0.05\lambda_0$, and its electrical permittivity usually varies between $2.2 \leq \varepsilon_r \leq 12$. Thick substrates with lower dielectric constants are favorable since they have higher efficiency and bandwidth. Whereas, when working at microwave frequency bands, thin substrates having higher dielectric constants can be more desirable as they minimize spurious radiation and coupling, and it enables the overall antenna size reduction. However, it leads to a trade-off between size and efficiency because of their higher power dissipation factor.

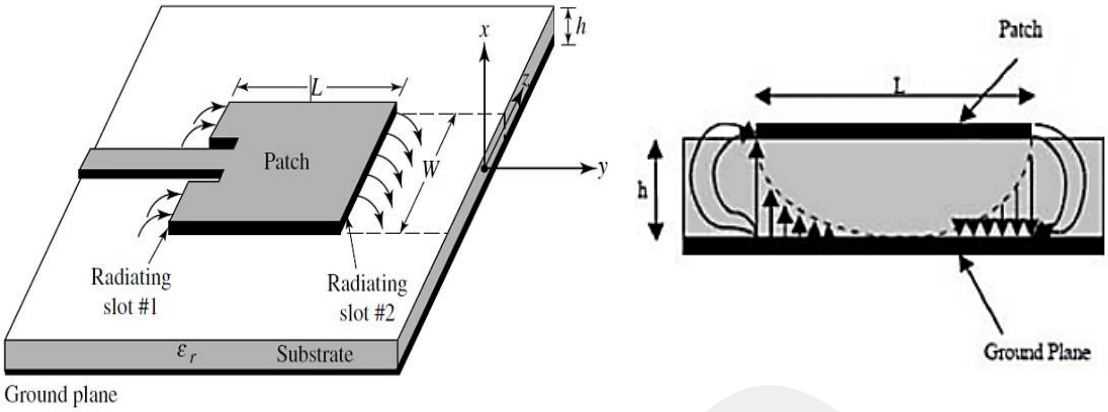

(a) (b)

Figure 2.1: Basic geometry of microstrip antenna: (a) Perspective view and (b) Side view [1]

When determining the patch configuration, there is a wide selection of patch shapes from square, rectangular, triangular, circular, elliptical, thin strip, spiral or any other formation by combination of different geometries. A patch is designed to obtain its maximum radiation pattern perpendicular to the patch. This phenomenon is achievable only if the proper mode of excitation is chosen. Decision on the type of shape is made depending on the operation band and the type of polarization. Rectangular and circular are the most used ones. Rectangular geometries are separable by nature and their analysis is simple, and they are quite suitable for linear polarization applications. On the other hand, circular patch shape is commonly used by generating 90-degree phase difference with two ports to produce circular polarization.

2.2 Feeding Techniques

There are many different feed techniques in the literature currently available. Feed methods can be divided mainly into two categories as contacting and non-contacting. Contacting method proposes the transmission of radio frequency power directly to the radiating patch by means of a connecting element, for example a microstrip line or the metal conductor inside a coaxial SMA connector. Non-contacting method uses an indirect contact scheme where electromagnetic field is coupled from microstrip line to the patch via a gap, a via hole or a slot, such as aperture coupling or proximity

coupling. Yet, four methods are the most frequently used ones, which are the microstrip line, coaxial probe, aperture coupling and proximity coupling, as discussed below.

2.2.1 Microstrip-Line Feed

Microstrip line feed method is one of the easiest to manufacture since it is only a conducting strip directly connecting to the patch. Its width is only of a fraction of patch width, and its matching to patch is simple with the aid of adjusting the inset position. While it can be impractical as the substrate thickness increases due to the increase in cross-polarized radiation and surface waves, limiting the bandwidth.

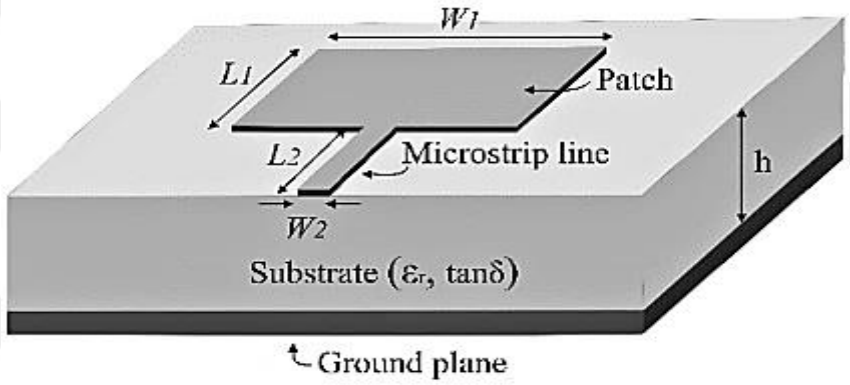

Figure 2.2: Microstrip-Line Feed Structure [1]

2.2.2 Coaxial Probe Feed

Coaxial feed method is another commonly used method by the designers, illustrated in Figure 2.3. It uses homocentric feeding technique in which the inner conductor is directly connected to the patch through a hole drilled in the substrate, and the outer teflon to the ground plane. This method is relatively easy to manufacture and to match if placed in the correct location in general terms. However, it comes with the expense of narrow bandwidth and the generation of undesired higher order modes causing cross- polarization, due to inaccuracies in drilling and soldering, making it harder technically for thicker substrates ($h > 0.02\lambda_0$).

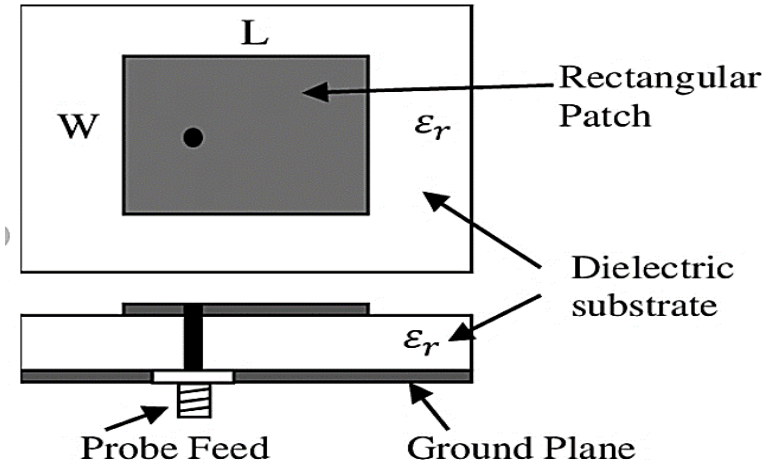

Figure 2.3: Geometry of Coaxial Probe Feed [50]

2.2.3 Aperture-Coupling Feed Method

This type of feeding is accepted as the hardest one to manufacture due to its multi-layered structure and it ends up with a narrow bandwidth. However, it can provide the lowest undesired radiation among the other feed methods. It basically consists of two substrates, a low dielectric thick substrate stacked on top of a high dielectric substrate as seen in Figure 2.4. A ground plane separates the two substrates. Microstrip feed line is used on a completely different layer, being underneath the lower substrate, and the radiating patch is placed on top of the upper substrate. Coupling between them is enabled via a slot placed on the ground plane which separates the two substrates. This type of designs offer freedom for minimizing interference of undesired radiation required for pattern formation and polarization purity by changing the location and dimensions of the aperture.

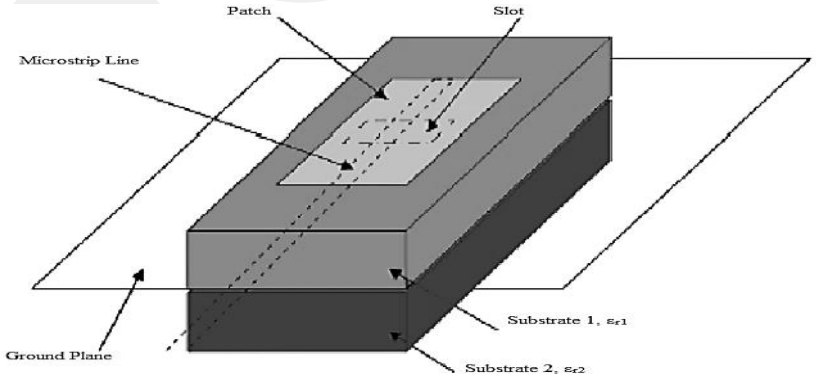

Figure 2.4: Aperture-Coupling Feed Geometry [1]

2.2.4 Proximity-Coupling Feed Method

Also known as electromagnetic coupling, this type of feed possesses the largest bandwidth of all the aforementioned feed methods, approximately as 13 percent. Additionally, it is easy to design and has moderate undesired feed radiation. Nonetheless it is difficult to manufacture due to its multi-layered complex structure. It is built similarly to aperture-coupling making use of two substrates with patch at the very top, but feed line is placed between the two substrates this time. Impedance matching can be accomplished by properly optimizing width to line ratio of patch and the length of microstrip feed line.

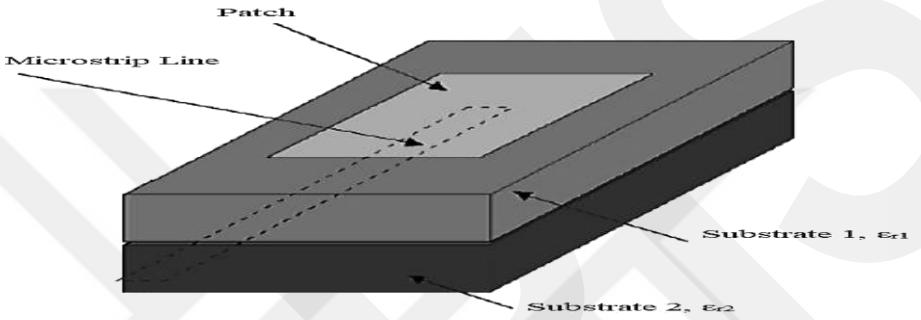

Figure 2.5: Proximity-Coupling Feed Geometry [1]

A brief comparison of feed techniques is presented in the following table 2 in terms of basic performance parameters.

Table 2.1: Comparison of feed methods

Parameter	Polarization Purity	Manufacture	Impedance Matching	Impedance Bandwidth
Strip-line	Moderate	Easy	Easy	2-5 %
Coaxial Probe	Moderate	Soldering and Drilling Needed	Difficult for Thicker Substrates	Narrow
Aperture-Coupling	Excellent	Symmetrical Alignment Needed	Difficult	Narrow
Proximity-Coupling	Moderate	Symmetrical Alignment Needed	Difficult	~ 13 %

2.3 Basic Antenna Performance Characteristics

In the way of assessing an antenna's operational behavior, some output parameters are crucial and should be discussed comprehensively. The most important key parameters for this study are return loss and voltage standing wave ratio (VSWR), directivity and gain, radiation pattern, radiation intensity, half-power beamwidth (HPBW), and antenna efficiency to be described in this section.

2.3.1 Return Loss and Voltage Standing Wave Ratio (VSWR)

In communication theory, return loss defines the loss of signal power because of the reflection originating from a discontinuity in a transmission line. This discontinuity can result from inaccuracies of impedance matching between the transmission line and load, or the input voltage source and transmission line. Return loss is derived from the reflection coefficient in electromagnetics theory and is related to voltage standing wave ratio as well. VSWR indicates the power efficiency of RF signal through a transmission line. Return loss and VSWR are inversely proportional to each other. Less than -10 dB for return loss and less than 2 for VSWR are the fundamental desired antenna performance indicators in general.

For the conversion of reflection coefficient to return loss in dB, the following formula can be used:

$$\mathrm{RL(dB)} = -20\log|\Gamma| \tag{2.1}$$

And the reflection coefficient is defined as the complex ratio between the reflected wave amplitude and the incident wave amplitude, which is expressed as follows:

$$|\Gamma| = \frac{v_0^-}{v_0^+} = \frac{z_L - z_0}{z_L + z_0} \tag{2.2}$$

where V_0^- represents the reflected wave and V_0^+ represents the incident wave, and Z_L represents the load impedance and Z_0 represents the characteristic impedance.

In order to perfectly match the transmission line and the radiating patch, the ideal condition is $\Gamma = 0$ and so $RL = \infty$, which expresses that there is no power reflected

back. But in practice, VSWR=2 corresponding to a return loss of -9.54 dB is satisfactory.

2.3.2 Directivity and Gain

The directivity of an antenna is defined for the specified boresight. If boresight is not specified directivity is said to be in the direction of the maximum radiated power. Directivity is known as the radiation intensity in a particular direction relatively to radiation intensity of isotropic antenna, which radiates unit Watt equally per solid angle (4π), and it can be calculated using the following formula:

$$D(\theta, \phi) = \frac{U}{\mathrm{U}_0} \tag{2.3}$$

and because of that,

$$\frac{dP_{rad}}{d\Omega} = U \tag{2.4}$$

and

$$\frac{P_{rad}}{4\Pi} = U_0 \tag{2.5}$$

Substituting 2.4 and 2.5 into 2.3 we obtain the following formula,

$$D(\theta, \phi) = \frac{dP_{rad}/d_{\Omega}}{P_{rad}/4\Pi} \tag{2.6}$$

where, U represents the radiation intensity, and D represents the directivity, and P_{rad} is the total radiated power.

If the direction is not stated, the direction of maximum radiation is defined as the direction of antenna directivity, and the formula below is used for that,

$$D(\theta, \phi) = \frac{U}{U_0} \tag{2.7}$$

Looking at gain, it is directly proportional to the directivity of an antenna. However, the main determining factor of gain is the antenna efficiency. As the antenna efficiency rises gain rises as well. It is defined as the total radiated power per unit solid angle divided by the input power, and by the following formula it can be calculated,

$$G(\theta, \varphi) = 4\pi \frac{dP_{rad}/d\Omega}{P_{in}} \tag{2.8}$$

To calculate the total radiated power by the antenna the following relation between the total input power and the antenna efficiency is used,

$$P_{rad} = \eta P_{in} \tag{2.9}$$

Antenna gain provides information on how well it illuminates a certain region by concentrating electromagnetic energy on that specific direction. It is expressed in dBi, taking isotropic radiator as reference. Directivity and gain are related to each other, and they are calculated by the following formula,

$$G(\theta, \varphi) = \eta D(\theta, \varphi) \tag{2.10}$$

2.3.3 Radiation Pattern

Radiation pattern, also called antenna pattern, is a projection of an antenna's radiated energy as a function of space coordinates, expressed in spherical coordinates (r**,** θ, φ). It is usually evaluated in the far-field (Fraunhofer) region. Radiation characteristics indicates an antenna's radiation intensity, directivity, power flux density, or for patch antenna arrays one can say whether the array is phased or not by referring to its radiation pattern. An antenna pattern is divided into two categories as field pattern on behalf of the diagram of magnitude of electric or magnetic field, and power pattern depicting the diagram of square of the magnitude of electric or magnetic field, and most practical antenna designs utilize from two-dimensional power pattern, and it is expressed in logarithmic scale (dB). A typical directional antenna pattern with its principal radiating planes is shown in the following figure 2.6.

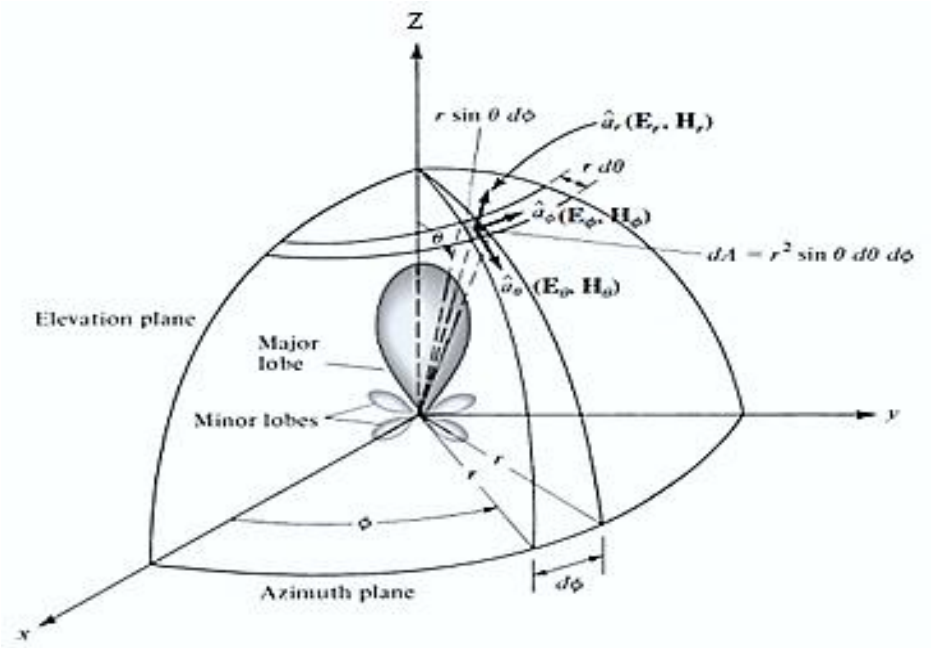

Figure 2.6: Antenna radiation pattern with its principal planes [1]

2.3.4 Radiation Intensity

Radiation intensity is the radiated power by an antenna per unit solid angle, and it is indicated as Watt per steradian. It is expressed as a far-field region parameter, and it is mathematically defined as follows:

$$U = r^2 W_{rad} \tag{2.11}$$

In the formula above U denotes the radiation intensity (W/unit solid angle), and W_{rad} symbolizes radiation density (W/m^2).

Radiation intensity is dependent on an antenna's electric field in far-field region as shown in the relationship below,

$$U(\theta, \phi) = \frac{r^2}{2\eta} \left|\vec{E}(r, \theta, \phi)\right|^2 \tag{2.12}$$

$$U(\theta, \phi) \approx \frac{r^2}{2\eta} \left(|E_\theta(r, \theta, \phi)|^2 + \left|E_\phi(r, \theta, \phi)\right|^2 \right) \tag{2.13}$$

$$U(\theta,\phi) \approx \frac{1}{2\eta}\left(|E_\theta(\theta,\phi)|^2 + \left|E_\phi(\theta,\phi)\right|^2\right) \quad (2.14)$$

In Equation 2.12, 2.13 and 2.14, E_θ and E_Φ denotes the antenna's far-zone electric-field components and η points out to the medium's intrinsic impedance.

The total radiated power from the antenna can be calculated by taking the integral of radiation density over the complete 4π solid angle by using the following formulas,

$$P_{rad} = \oiint_S \vec{W}_{rad} \cdot d\vec{s} = \oiint \frac{U}{r^2}(r^2 \sin\theta d\theta d\phi) \quad (2.15)$$

and,

$$P_{rad} = \int_0^{2\pi}\int_0^{\pi} U \sin\theta \, d\theta \, d\phi = \oiint_\Omega U d\Omega \quad (2.16)$$

where $d\Omega = \sin\theta d\theta d\Phi$, $d\Omega$ is the differential solid angle.

2.3.5 Half-Power Beamwidth (HPBW)

Half power beamwidth is defined as the angle between the two points where the maximum value of the radiation intensity falls to its one-half value, in the principal plane containing the direction of its maximum radiation intensity. For pencil beam antenna investigations narrowing down the HPBW is significant, and they are served to identify exceedingly small objects, human beings or spacing between them. In practice, the term beamwidth is used instead of HPBW in general.

- Main beam or also called major lobe of an antenna is defined as the part of the radiation pattern carrying the maximum radiation intensity in the targeted direction radiated by the antenna.
- A minor lobe is defined as any lobe apart from the major lobe, and they are undesired, because they scatter the radiated energy in undesired directions. In linear patch arrays, as the number of patch elements increases the number of sidelobes increases. For sidelobe-level suppression, patch excitation amplitude weighting methods are being used such as Taylor and Chebyshev distribution.

- A back lobe is observed as the radiation lobe 180 degrees opposite to main lobe, it usually carries significantly low amount of energy that can be neglected. The figure 2.7 exhibits a common three-dimensional unidirectional radiation pattern and a linear plot of power pattern for clarification of beamwidth and the associated lobes.

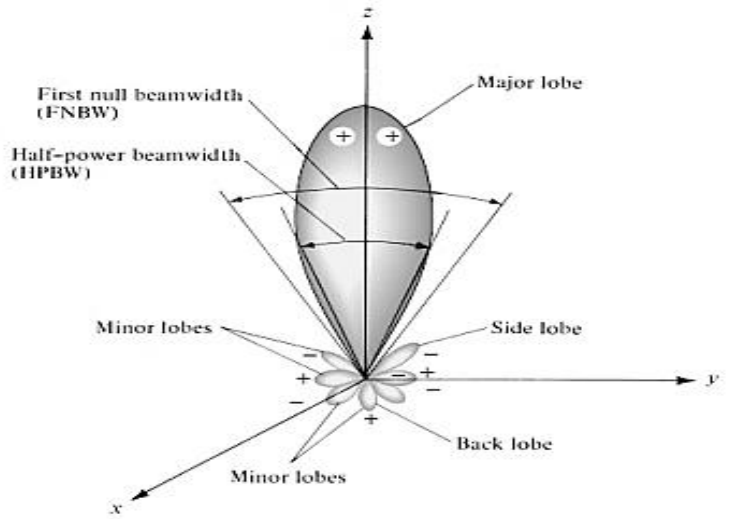

(a)

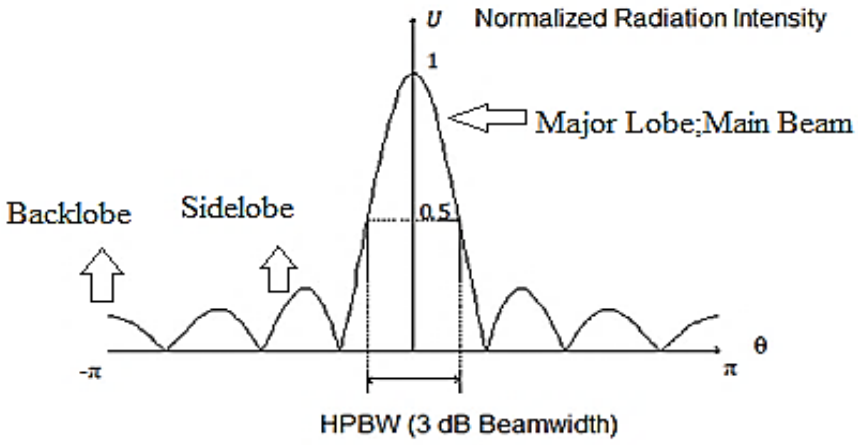

(b)

Figure 2.7: (a) 3D Radiation lobes and beamwidth in Cartesian coordinates and (b) 2D Rectilinear radiated power pattern plot [1]

2.3.6 Antenna Efficiency

The overall antenna efficiency takes into consideration several losses such as the impedance mismatch between the transmission line and load (radiating patch), ohmic losses due to the dielectric material selection and conduction losses that can arise from conducting material selection like aluminum or copper. In addition, thermal efficiency of an antenna, a factor contributing to antenna noise temperature, can affect the overall efficiency.

$$e_0 = e_r e_c e_d \tag{2.17}$$

Equation 2.17 defines the total antenna efficiency mathematically, where e_0 expresses the total efficiency, e_r indicates matching (reflection) efficiency, e_c denotes conduction efficiency and e_d is dielectric efficiency. Though conduction and dielectric efficiencies are hard to compute via simulation, their existence can be proven with the aid of experimental antenna measurements, but still, it is difficult to distinguish between them, hence they are expressed as a joint single term as e_{cd}. Therefore, the following equations are more useful in practice.

$$\mathrm{e_r} = (1 - |\Gamma|^2) \tag{2.18}$$

$|\Gamma|^2$ is the voltage reflection coefficient, and substituting 2.18 into 2.17 we have,

$$\mathrm{e_0} = \mathrm{e_r e_{cd}} = \mathrm{e_{cd}}(1 - |\Gamma|^2) \tag{2.19}$$

100 % antenna efficiency is impossible to achieve, because a transmission line is always lossy and the maximum power transfer from the input power source can never be completely radiated by the antenna due to the previously mentioned losses. Antenna efficiency in terms of input power and radiated power can be expressed mathematically as in the following equations.

$$\mathrm{P_{rad}} = \eta_\mathrm{e} \mathrm{P_{in}} \tag{2.20}$$

$$\eta_\mathrm{e} = \frac{\mathrm{P_{rad}}}{\mathrm{P_{in}}} \tag{2.21}$$

η_e is the overall antenna efficiency, P_{rad} the radiated power and P_{in} is input power.

2.4 Antenna Arrays

A single element antenna tends to have a wide beam with a low directivity and gain. Its main beam is focused on a fixed direction and if beam steering is desired at multiple frequencies, mechanical beam steering by moving the antenna or computer aided phase shifters are required to achieve several beams in varying directions simultaneously. These limitations can be managed by laying multiple antenna elements out in a precise configuration such as a straight line or circle or triangle arrangement. These types of formations made of antenna elements are defined as antenna arrays. Because of that this study focuses on array antenna design and operation, basic theoretical information and characteristics on uniform phased linear arrays, scanning arrays and Chebyshev arrays are provided throughout this section.

2.4.1 N-Element Linear Array

Considering an array of N antenna elements equally spaced aligned along the same axis, if each element is excited with the same current amplitude and have the same phase shift between each two successive elements, such an array is defined as a uniform linear array. Owing to the identical element dimensions and equidistance between them, the total electric field produced by the array is calculated by multiplying the array factor with the electric field of a single element. This rule is based on the pattern multiplication theory of an array.

$$E_t = (Element\ factor) \times (Array\ factor) = E_0 \times AF(\psi) \tag{2.22}$$

$$AF = 1 + e^{j(kd\cos\theta+\beta)} + e^{j2(kd\cos\theta+\beta)} + \cdots + e^{j(N-1)(kd\cos\theta+\beta)} \tag{2.23}$$

where, β represents the phase difference or phase shift, d is the spacing between each successive two elements and N is the total number of array elements. Array factor can be found by the following exponential summation formula.

$$AF = \sum_{n=1}^{N} e^{j(n-1)(kd\cos\theta+\beta)} \tag{2.24}$$

And if,

$$\psi = kd\cos\theta + \beta \tag{2.25}$$

substituting 2.25 into 2.24 yields the following equation,

$$\mathrm{AF} = \sum_{n=1}^{N} e^{j(n-1)\psi} \tag{2.26}$$

And 2.23 is transformed into the following equation,

$$\mathrm{AF} = 1 + e^{j\psi} + e^{j2\psi} + \cdots + e^{j(N-1)\psi} \tag{2.27}$$

where,

Ψ: progressive phase relative to the prior one

d: distance between consecutive elements

θ: elevation angle

β: phase delay between each two successive elements

k: wave number, shown as ($k = 2\pi/\lambda$)

The general structure of a linear uniform array is presented as an outline in the figure below.

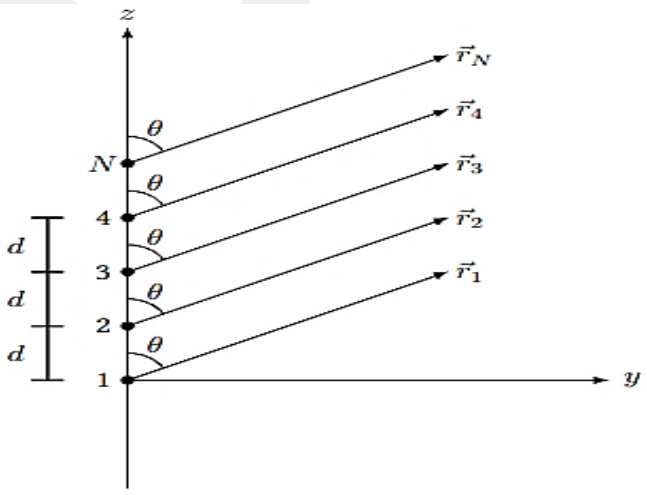

Figure 2.8: Far-field geometry of N-element uniform isotropic source array aligned on the z-axis [51]

2.4.2 Frequency Scanning Phased Array

The frequency scanning array is included in the subcategory of phased array antenna. The beam steering is provided by varying the transmitter's frequency of operation, and it is achieved without making use of any phase shifter. This type of scanning arrays is currently in strong demand by automakers due to its simultaneous beamforming capabilities in different spatial directions to be used for angular scanning purposes at sensors. As a result of electronical beam steering there is no need for mechanical steering anymore.

A scanning array is usually serially fed, and all the radiating elements are in-phase at the main resonance frequency F_0. Therefore, the elements radiate with the same phase and the maximum radiation intensity is produced alongside the axis on which the array is positioned similar to an endfire array (θ=0°or θ=180°). The resulting maximum main lobe is normal to the antenna's plane.

However, when the transmitter's operating frequency is switched upwards to a new frequency F_1, the guided wavelength drops and the same detour path it must cross over between the radiating elements becomes a bit too longer than the nominal case of the operating frequency F_0. Consequently, a phase delay arises from one radiating element to the next one. The first element radiates a bit too earlier than the next adjacent radiator, thereby producing a main beam steered by the angle θ_S. As a result, by controlling the spacing between the neighboring radiating elements, phase shift between them can be controlled and so the resultant beam can be steered accordingly. The following relations are beneficial to calculate the phase shift between the elements.

$$x = d \sin \vartheta_S \tag{2.28}$$

$$\frac{360^0}{\Delta\varphi} = \frac{\lambda_g}{x} \tag{2.29}$$

$$\Delta\varphi = \frac{360^0 d \sin \theta_s}{\lambda_g} \tag{2.30}$$

where, d is the distance between each two neighboring elements, θ_S is the steering angle, λ_g is the guided wavelength, and $\Delta\varphi$ is the phase delay between the two neighboring elements.

2.4.3 Dolph-Chebysheff Weighting Array

Chebysheff weighting method is used to optimize all the sidelobe levels of an array antenna by equalizing all the sidelobes in magnitude. This method is achieved by lowering the higher sidelobes while raising the lower sidelobes, in short, aligning all the sidelobe levels at the same level, for a given beamwidth. Contrarily, for a particularly desired sidelobe level Chebyshev calculates the smallest beamwidth possible. This method was found by Dolph in 1946 and further investigation was conducted by others [1,15-19]. It is a nonuniform amplitude distribution model by means of amplitude tapering along the excitation source.

Chebyshev response has equal ripples oscillating between [-1,1], and these oscillations are equal in magnitude. The logic is to use these polynomials with certain coefficients and to match them to the array factor.

If we assume we have a symmetric antenna array uniformly spaced with distance 'd', then the array factor for even array can be written as:

$$AF = \sum_{n=1}^{M} \omega_n e^{-jk(2n-1)\frac{d}{2}\cos\theta} + \sum_{n=-M}^{-1} \omega_n e^{-jk(2n-1)\frac{d}{2}\cos\theta} \tag{2.31}$$

Where w_n represents the weight, and for odd array it is of the form:

$$AF = \sum_{n=-M}^{M} w_n e^{-jknd\cos\theta} \tag{2.32}$$

The array is called even if there are even number of radiating patch elements, and it is called odd if the number of radiating elements is odd. Using the Euler's formula for the cosine function:

$$\cos(x) = \frac{e^{jx} + e^{-jx}}{2} \tag{2.33}$$

Substituting the above cosine function 2.33 into 2.31 and 2.32, we have the following:

$$AF = \sum_{n=1}^{M} w_n \cos[(2n-1)u] \tag{2.34}$$

for even array, and for odd array we have the following:

$$AF = \sum_{n=0}^{M} w_n \cos(2nu) \tag{2.35}$$

where u = kdcosθ/2. To match these equations to Chebyshev polynomials we assume z = cosu, and the expansion of cosine terms regarding trigonometric identities should be recalled as in the following set of equations:

$$\begin{gathered} m = 0, cos(mu) = 1 = T_0(z) \\ m = 1, cos(mu) = cosu = z = T_1(z) \\ m = 2, cos(mu) = cos(2u) = 2\,cos^2 u - 1 = 2z^2 - 1 = T_2(z) \\ m = 3, cos(mu) = cos(3u) = 4\,cos^3 u - 3\,cos\,u = 4z^3 - 3z = T_3(z) \\ m = 4, cos(mu) = cos(4u) = 8\,cos^4 u - 8\,cos^2 u + 1 = 8z^4 - 8z^2 + 1 = T_4(z) \\ m = 5, cos(mu) = cos(5u) = 16\,cos^5 u - 20\,cos^3 u + 5\,cos\,u = 16z^s - 20z^3 + \\ 5z = T_5(z) \end{gathered} \tag{2.36}$$

where m denotes an integer and u represents the fundamental operating frequency, and the above series of cosine functions-Chebyshev polynomial ($T_m(z)$) relations, can go on according to the order of the polynomial, which is always one less than the number of array elements. And these relations are only valid for the interval $-1 \leq z \leq +1$, because each Chebyshev polynomial is $|T_m(z)| \leq 1$ for this range. While, for $|z| > 1$, hyperbolic cosine functions are used to find the excitation coefficients. The following recursion relation defines the m'th order Chebyshev polynomial:

$$T_m(z) = 2zT_{m-1}(z) - T_{m-2}(z), \qquad m = 2,3,\ldots \tag{2.37}$$

Substituting the trigonometric expressions in 2.36 into the array factors in 2.34 or 2.35, and by substituting cos(u) with z/z_0, the resulting polynomial can be matched to corresponding Chebyshev polynomial '$T_m(z)$' of m'th order, where m is one less than

the number of array elements, and by finding the resultant set of equations the corresponding weights or excitation coefficients 'w_n' can be obtained. Lastly, there are two issues to be emphasized on Chebyshev arrays:

- For a specified sidelobe level, the directivity grows steadily as the number of array elements increase.
- For a given number of array elements, the directivity does not always rise as the sidelobe level drops down.

2.5 Analysis Method for Rectangular Patch Antenna

There are several analysis methods to be utilized for microstrip patch antennas currently. Transmission line model, cavity model and full-wave model are by far the most common analysis methods. However, they vary in accuracy and complexity. The transmission-line model is the most straightforward of all, offering clear physical insight, at the expense of its insufficient accuracy. The cavity model provides more accurate results relatively to the transmission-line model, yet it is quite complex to model. The full-wave models are accepted as the most accurate and practical of all, leading them to be used at commercial electromagnetics analysis softwares. However, apart from their use at simulators, they are far too complex to use when calculating by hand, because they are based on extraordinarily complex iterative numerical techniques like finite-element method (FEM) or finite integration technique (FIT). Consequently, this thesis considers the full-wave analysis via FEM based HFSS as a comprehensive parametric study, subsequently to transmission-line model analysis as a preliminary investigation.

2.5.1 Transmission-Line Model Analysis

This model takes two slots and a transmission line, on behalf of the microstrip antenna, the slots are separated by a transmission line of length 'L' and of width 'W' and of impedance 'Z_c' which is placed on a dielectric substrate of height 'h' and of electrical permittivity 'ε_r'. The slots of the patch at each end have remarkably high impedance causing the edges to behave like an open circuit, and therefore the patch exhibits a significantly resonant characteristic as a function of its length 'L'. The field lines at the edges of the patch are exposed to a phenomenon called fringing effect, which

causes the patch to look electrically larger than its physical size. These field lines travels through a nonhomogeneous medium comprised of two dielectrics, which are substrate and air. A part of the waves settles in the substrate while some travels in the air as a function of the patch length to substrate height ratio (L/h), patch width to substrate height ratio (W/h) and the relative permittivity of the substrate (ε_r). This situation has a serious effect on the excitation mode of transmission line, resulting in quasi-transverse electromagnetic (quasi-TEM) mode propagation instead of pure TEM mode. It arises from the different phase velocities of propagation due to different resistivities and losses of air and substrate leading to nonuniform wave propagation. Therefore, generating pure TEM mode is impossible in real life. In addition, rising the substrate thickness leads to the increase in the amount of fringing, ending up with larger separations between the electronical dimensions of the patch edges and a lower resonance frequency. As a result, an effective dielectric constant 'ε_{reff}' must be calculated to count in the fringing effect. The following figure illustrates a typical microstrip transmission line and the dissipation of its electric field lines.

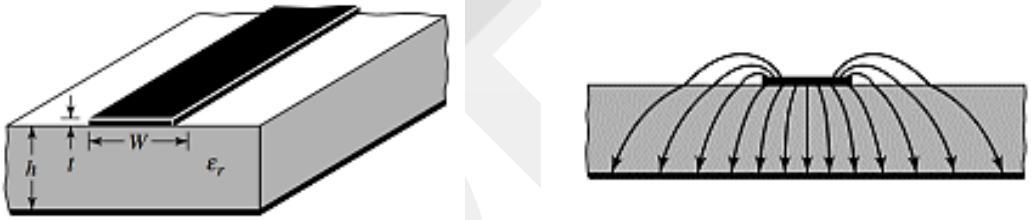

Figure 2.9: (a) Microstrip transmission line and (b) Regarding electric field lines [1]

The effective dielectric constant value lies in the interval of $1 < \varepsilon_{reff} < \varepsilon_r$. When the substrate permittivity is much greater than one ($\varepsilon_r >> 1$) as it is in most cases, 'ε_{reff}' approaches to the actual value of permittivity 'ε_r'. Also, it is proportional to the operating frequency. The higher the operating frequency is, the more electric field waves reside in the substrate, causing the transmission line to behave almost like a homogeneous line of only one dielectric (substrate). Therefore, as the resonance frequency increases the effective dielectric constant draws closer to the actual dielectric constant value of the substrate. The following relation of the effective dielectric constant can be used during the calculations for when W/h > 1,

$$\varepsilon_{reff} = \frac{\varepsilon_r + 1}{2} + \frac{\varepsilon_r - 1}{2}\left(1 + 12\frac{h}{W}\right)^{-0.5} \quad (2.38)$$

ε_{reff} : effective dielectric constant of substrate

h: substrate height

W: transmission line or patch width

ε_r: relative dielectric constant (electrical permittivity) of substrate

The microstrip antenna patch looks electrically larger than its actual size by virtue of fringing effect, resulting in the extension of resonant patch on both sides by ΔL, as described in the figure below.

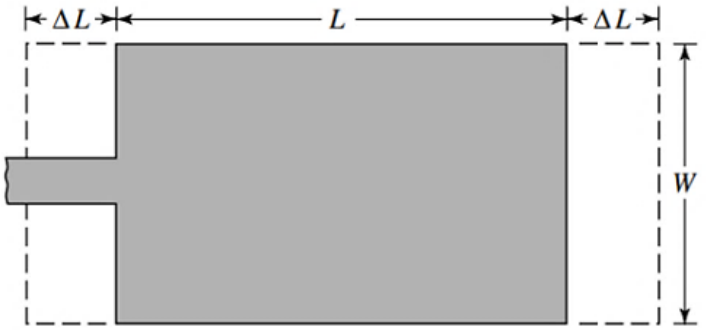

(a)

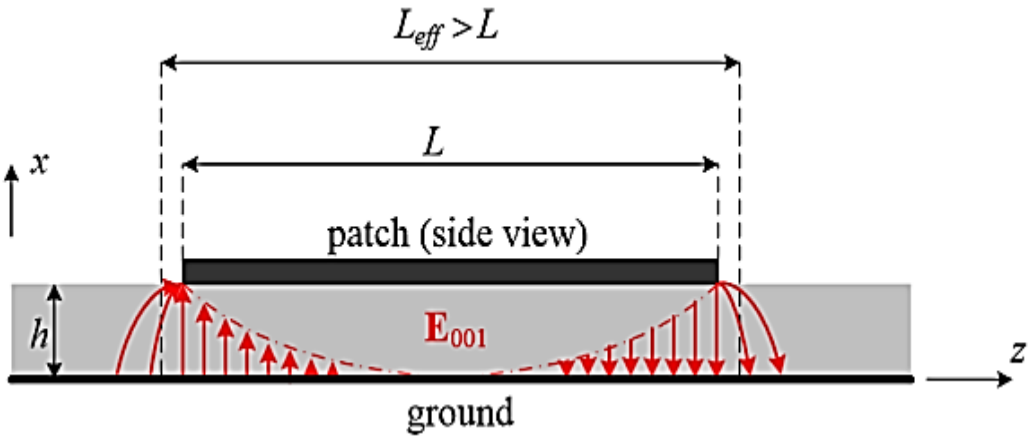

(b)

Figure 2.10: (a) Front view and (b) Side view geometry of actual length and effective length of patch antenna exposed to edge effect [1]

The length extension ΔL of the patch can be calculated through the following equation,

$$\Delta L = 0.412h\frac{\left(\varepsilon_{reff}+0.3\right)\left(\frac{W}{h}+0.264\right)}{\left(\varepsilon_{reff}-0.258\right)\left(\frac{W}{h}+0.8\right)} \tag{2.39}$$

Because of that incremental length extends on both sides of the patch, the effective resonance length of patch can now be determined by the addition of twice the length extension to the actual length, as formulated below.

$$L_{eff} = L + 2\Delta L \tag{2.40}$$

To calculate the resonance frequency of the rectangular patch antenna, patch length and edge effect should be taken into consideration, and for transverse magnetic (TM_{010}) mode excitation, it is expressed as,

$$(f_{rc})_{010} = q\frac{c}{2L\sqrt{\epsilon_r}} = \frac{c}{2L_{e_{ff}}\sqrt{\epsilon_{reff}}} \tag{2.41}$$

and q is defined as the 'fringe factor', which can be found by,

$$\mathrm{q} = \frac{(\mathrm{f_{rc}})_{010}}{(\mathrm{f_r})_{010}} = \frac{\frac{\mathrm{c}}{2\mathrm{L_{e_{ff}}}\sqrt{\epsilon_{\mathrm{reff}}}}}{\frac{\mathrm{c}}{2\mathrm{L}\sqrt{\epsilon_{\mathrm{r}}}}} = \frac{\mathrm{L}\sqrt{\epsilon_{\mathrm{r}}}}{\mathrm{L_{e_{ff}}}\sqrt{\epsilon_{\mathrm{reff}}}} \tag{2.42}$$

Lastly, after specifying the operating frequency and the selection of dielectric substrate material, the approximate width of the patch can be determined by the formula below,

$$W = \frac{c_0}{2f_r}\sqrt{\frac{2}{\varepsilon_r+1}} \tag{2.43}$$

where, 'c' is the speed of light in free space or in vacuum, c_0 = 299792458 m/s.

CHAPTER 3

DESIGN AND PARAMETRIC STUDY

A series-fed linear patch array is studied at the center frequency of 76.5 GHz as the first stage. Because of mmWave antennas cannot be fed with a conventional SMA connector, the recent studies in the literature propose to use waveguide feeding. However, designing the proper passive components such as transition structures between the waveguide and strip line is still quite difficult. Therefore, the emphasis is mostly on the design of ground-signal-ground (GSG) padding as the transition structure at the first stage. Following that, shorting pins are loaded to the GSG pad for gain enhancement to make the antenna compatible with medium-range or long-range purposes. At the second stage, a technique is proposed to convert 76.5 GHz linear patch array into 79 GHz linear array by adjusting the spacings between each two adjacent array elements. The main argument for this proposal is based on setting the phase delays between the array elements appropriately to the wavelength variation due to the increase in operating frequency. A comparative analysis between the first stage and the second stage performance characteristics is conducted lastly.

3.1 Linear Patch Antenna Array Design at 76.5 GHz

3.1.1 Design Without Shorting Via

To begin with, theoretical dimension calculations are performed for a single resonant rectangular patch element etched on RO3003 substrate of 0.127 mm (5 mil) thickness and with relative permittivity of $\varepsilon_r = 3$, and dielectric tangential loss (dissipation factor) is 0.0013, at 76.5 GHz with the aid of transmission-line model analysis to obtain an approximate estimation prior to simulations in HFSS, as presented in the table below.

Table 3.1: Transmission-line model calculations of 76.5 GHz antenna

Parameters	Value
Width (mm)	1.3855
Effective Dielectric Constant	2.6901
Actual Length (mm)	1.0719
Effective Length (mm)	1.1947

Table 3.1 (continued)

Guided Wavelength (mm)	2.3893
Free Space Wavelength (mm)	3.9189
Resonance Frequency (GHz)	76.4976
Fringe Factor ('q')	0.9475

After the preliminary theoretical estimations, [15] is determined as a reference source for the initial dimensions of patch and substrate, and it is simulated in HFSS. The horizontal patch geometry (as width and length) and its dimensions as sixteen element linear array configuration with series feed is presented in the figures and tables below.

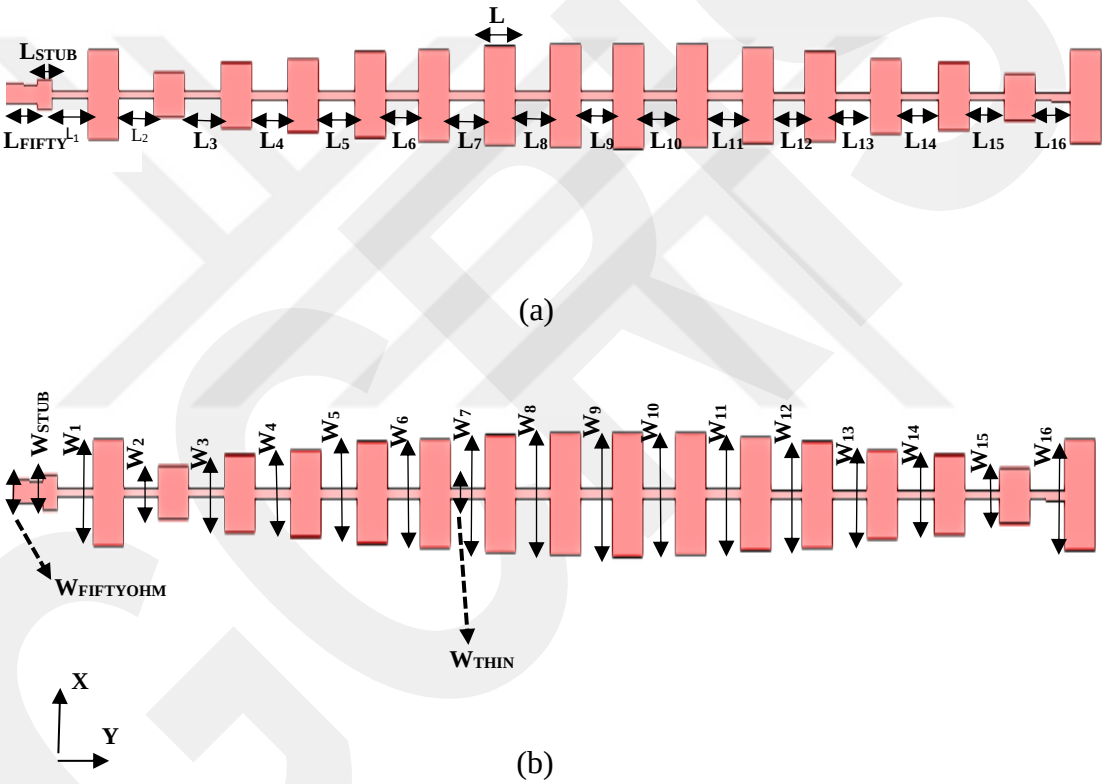

Figure 3.1: Top view geometry of reference sixteen element linear array:
(a) Dimensions of length (y-axis) and (b) Dimensions of width (x-axis) [15]

Table 3.2: Dimensions of spacings between the array elements (in mm) [15]

L_1	1.24	**L_5**	1.25	**L_9**	1.1	**L_{13}**	1.2
L_2	1.2	**L_6**	1.15	**L_{10}**	1.15	**L_{14}**	1.3
L_3	1.25	**L_7**	1.2	**L_{11}**	1.2	**L_{15}**	1.2
L_4	1.24	**L_8**	1.2	**L_{12}**	1.08	**L_{16}**	1.2

Table 3.3: Length dimensions of array elements, quarter-wave impedance transformer (matching stub), and 50 Ω feed line

L (all sixteen elements)	**L_{STUB}**	**L_{FIFTY}**
1.08 mm	0.52 mm	1.15 mm

Table 3.4: Width dimensions of array elements (in mm)

W_1	1.22	**W_5**	1.19	**W_9**	1.45	**W_{13}**	1.05
W_2	0.62	**W_6**	1.27	**W_{10}**	1.42	**W_{14}**	0.93
W_3	0.9	**W_7**	1.38	**W_{11}**	1.31	**W_{15}**	0.65
W_4	1	**W_8**	1.4	**W_{12}**	1.24	**W_{16}**	1.3

Table 3.5: Width dimensions of thin feed line, quarter-wave impedance transformer (matching stub), and 50 Ω feed line

W_{THIN} (same throughout the whole array)	**W_{STUB}**	**$W_{FIFTYOHM}$**
0.12 mm	0.4 mm	0.28 mm

Because of the lack of GSG padding dimensions in the reference article, an in-depth study is conducted to first approximately find out and then optimize these values, and so the regarding transition geometry and the optimized values are presented below.

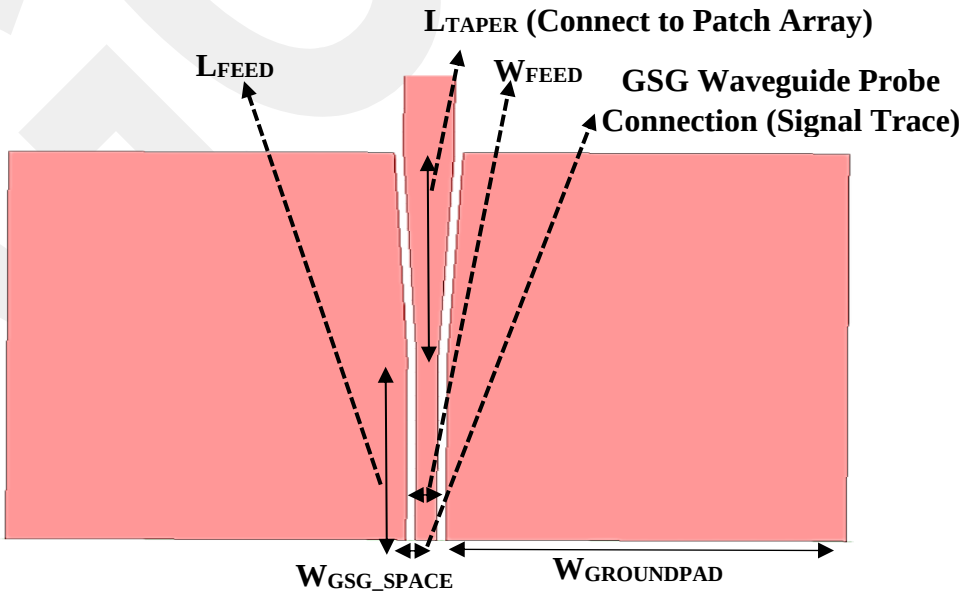

Figure 3.2: Top view geometry of GSG padding to microstrip line transition structure

Table 3.6: Optimized dimensions of GSG padding transition structure

L_{FEED}	L_{TAPER}	W_{GSG_SPACE}	W_{FEED}	$W_{GROUNDPAD}$
1.48 mm	1.68 mm	50 µm	0.12 mm	1.98 mm

The spacing between the central signal trace and each ground pad is kept at 50 µm due to the minimum spacing distance the optical lithography manufacturing technique allows [44]. Nonetheless, smaller spacing is observed to contribute to bandwidth during the simulations. While determining the tapered transmission line length, referring to transmission line theory the initial minimum estimation is chosen around the three times the quarter wavelength (3λ/4), as an odd multiple of quarter wavelength, to ensure that probe connecting transmission line impedance is correctly matched to 50 Ω line impedance connecting to load (radiating patch array) to prevent undesired reflections [45]. Also, longer tapering feed line is observed to cause gain loss, so its length is optimized in accordance with the input transmission line length. As a result, the lengths of these two sections of transmission line are optimized in proportion to each other.

The substrate dimensions are kept as small as possible as shown in the following Figure 3.3 and Table 3.7.

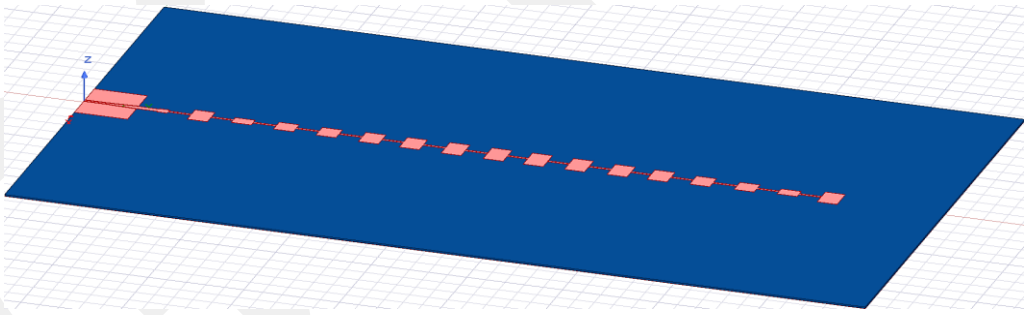

(a)

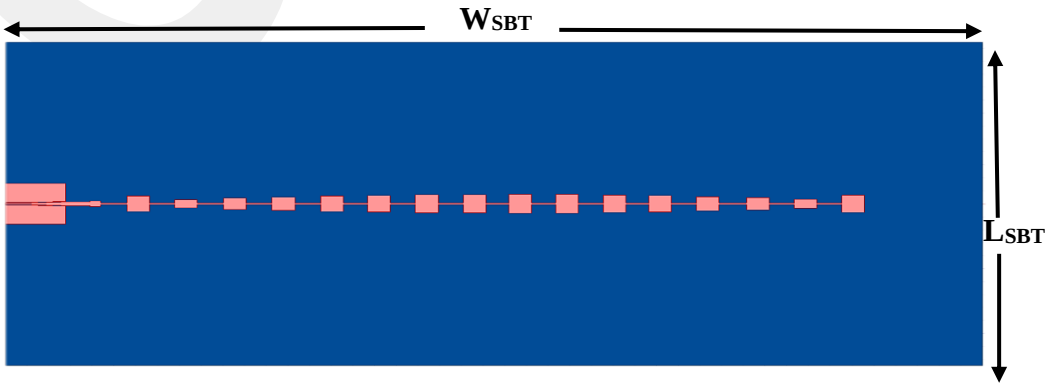

(b)

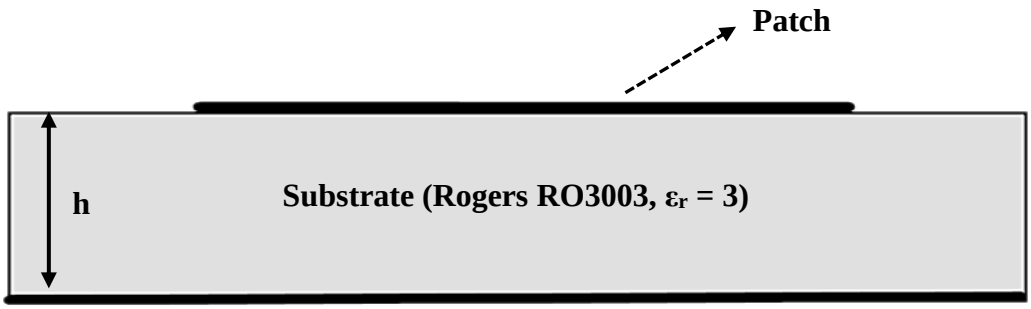

25x45 mm Ground

(c)

Figure 3.3: Geometry of linear array antenna: (a) 3-D perspective view (b) top view and (c) side view

Table 3.7: Dimensions of dielectric substrate

W_{SBT}	L_{SBT}	h
25 mm	45 mm	0.127 mm

Input transmission line width (W_{FEED}) is remained the same as the width of thin line (W_{THIN}) passing through the array elements to keep the whole array in phase. In addition, it is observed that the width of ground pads ($W_{GROUNDPAD}$) significantly affects the bandwidth, thus it is optimized to obtain the bandwidth of reference article. The effect of waveguide feed probe connecting line length is demonstrated with the simulation results in the figures below (L_{FEED}).

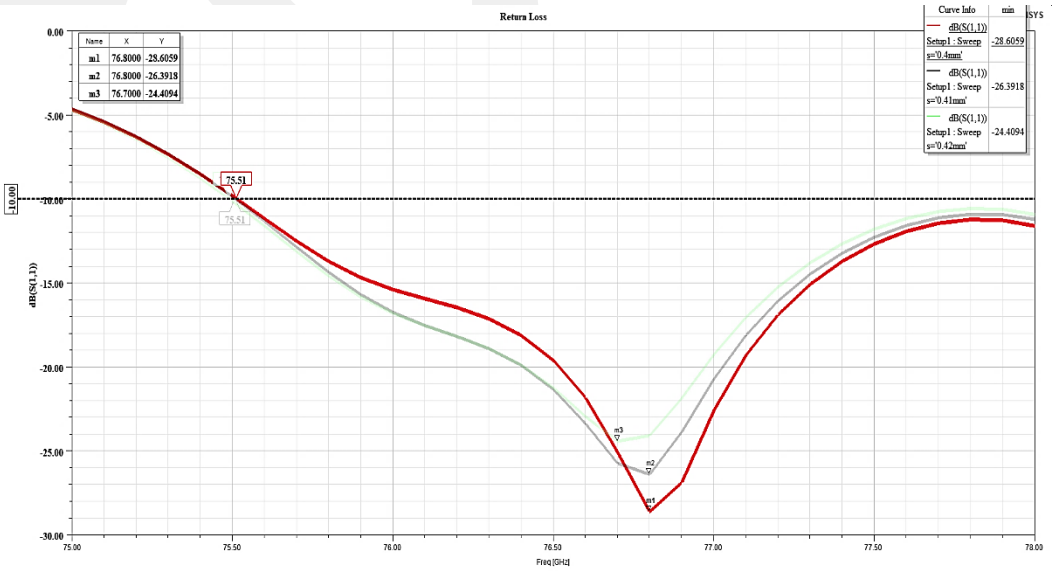

Figure 3.4: Return loss of varying input feed probe connecting line length (L_{FEED})

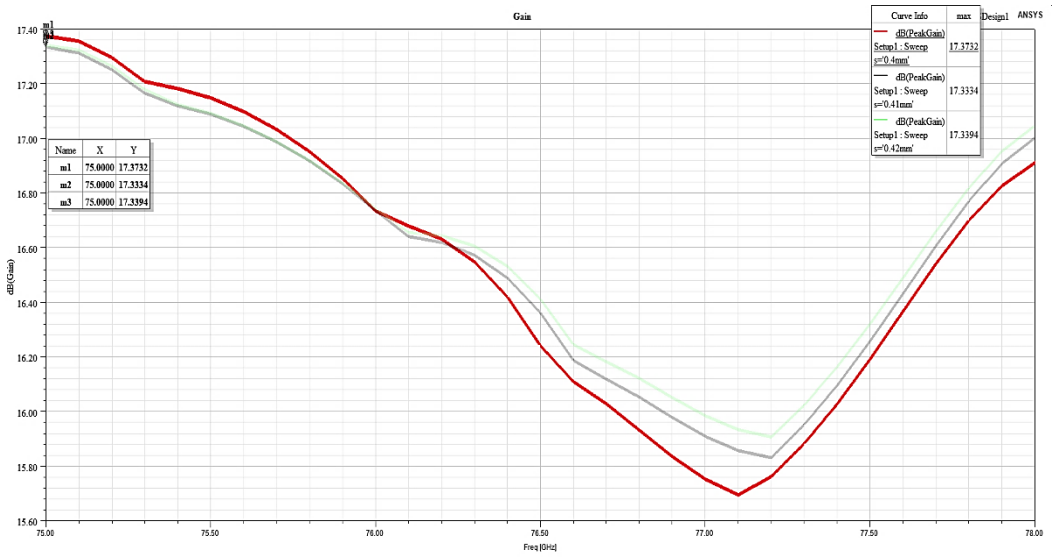

Figure 3.5: Gain vs. frequency of varying input feed connecting line length (L_{FEED})

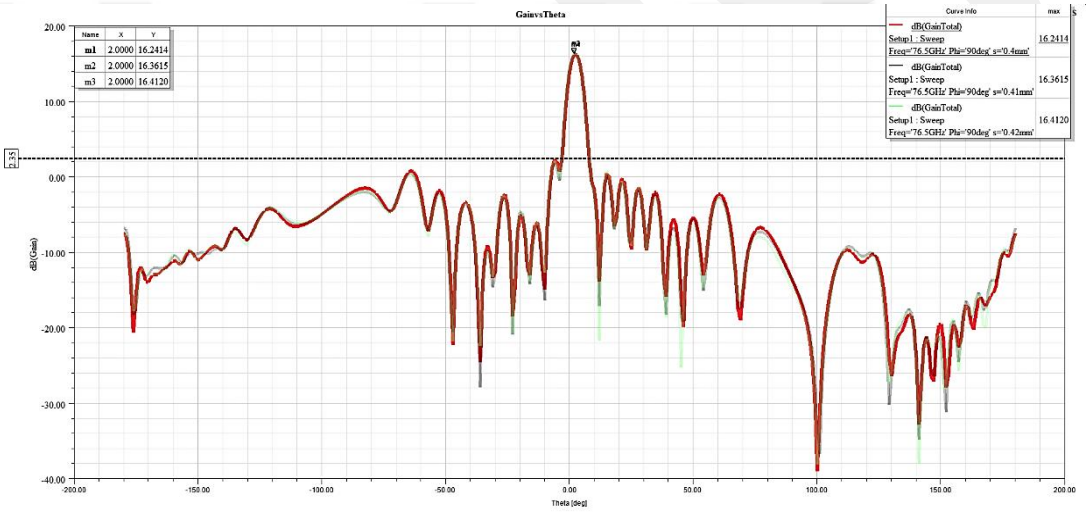

Figure 3.6: Gain versus theta of varying input feed probe connecting line length (L_{FEED}) in elevation (y-z plane) and at 76.5 GHz

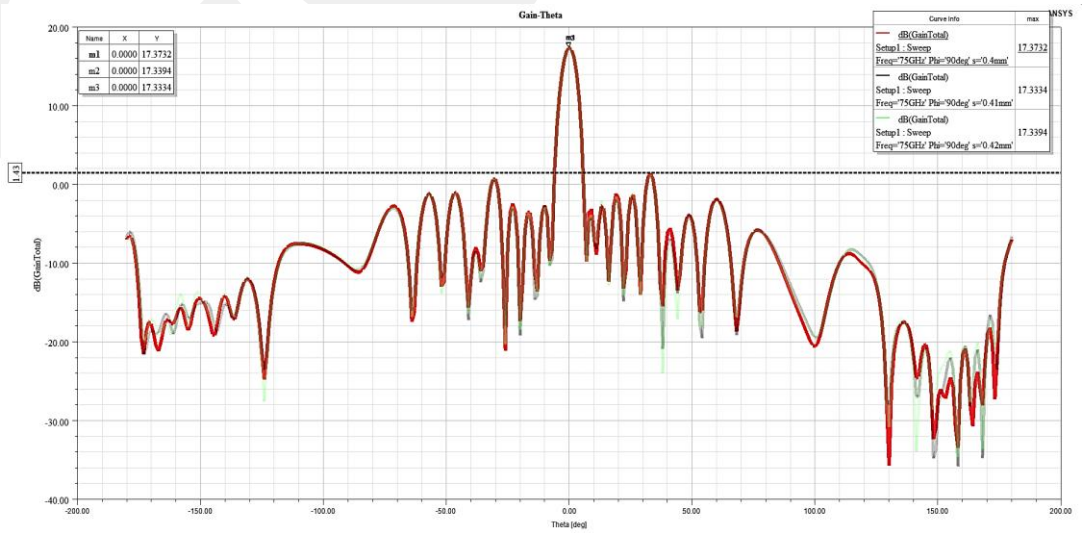

Figure 3.7: Gain versus theta of varying input feed probe connecting line length (L_{FEED}) in elevation (y-z plane) and at 75 GHz

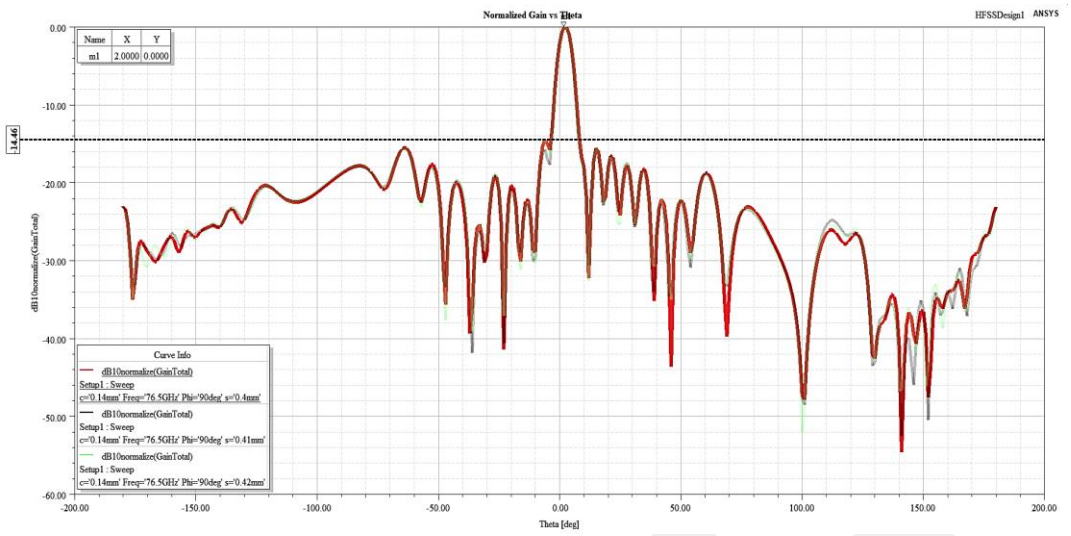

Figure 3.8: Normalized gain versus theta of varying input feed probe connecting line length (L_{FEED}) in elevation (y-z plane) and at 76.5 GHz

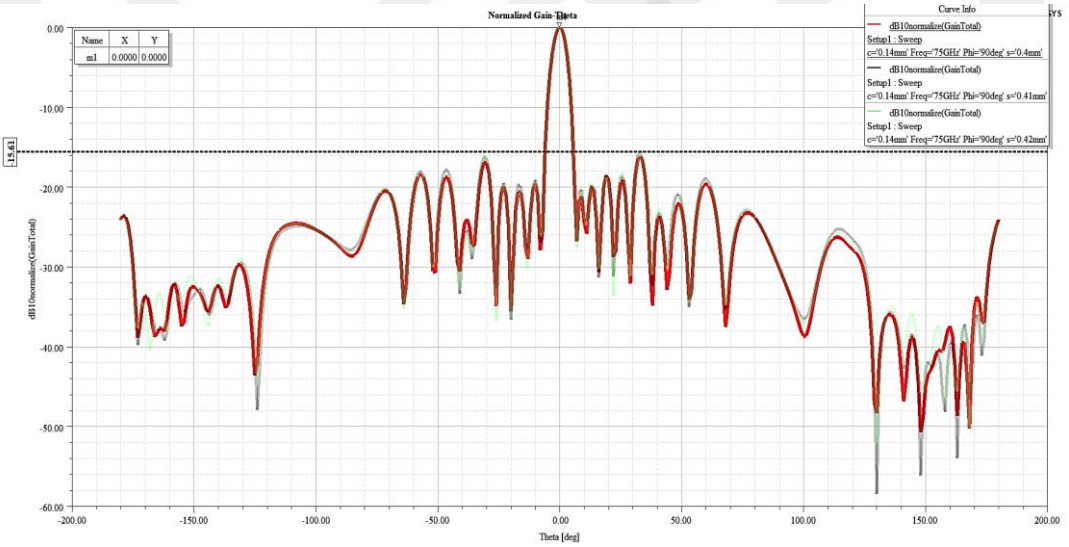

Figure 3.9: Normalized gain versus theta of varying input feed probe connecting line length (L_{FEED}) in elevation (y-z plane) and at 75 GHz

The direct effect of input feed line length on the resonance frequency and the gain is exhibited in the graphs above. Return loss shows that as the line length is shortened the resonance frequency rises. And from the gain versus frequency graph, it is observed that shorter line length yields higher peak gain at about 17.37 dBi. It is known that the transmission line width determines the characteristic impedance and, the length determines the phase (electrical length) and, the generated phase delay should be at around 180° to minimize the undesired reflections [45]. Hence, because the width is given in the article, the length is optimized according to the 180° phase shift principle. In addition, from the normalized gain versus theta graph 2° shift in theta is

observed at 76.5 GHz, however, the pattern is precisely centered at 0° in theta at 75 GHz in E-plane (y-z). Sidelobe level (SLL) of -14.46 dB at 76.5 GHz and, of -15.61 dB at 75 GHz is achieved at this stage.

The next stage relates to the effect of tapered transmission line length as shown in the figures of simulation results below (L_{TAPER}).

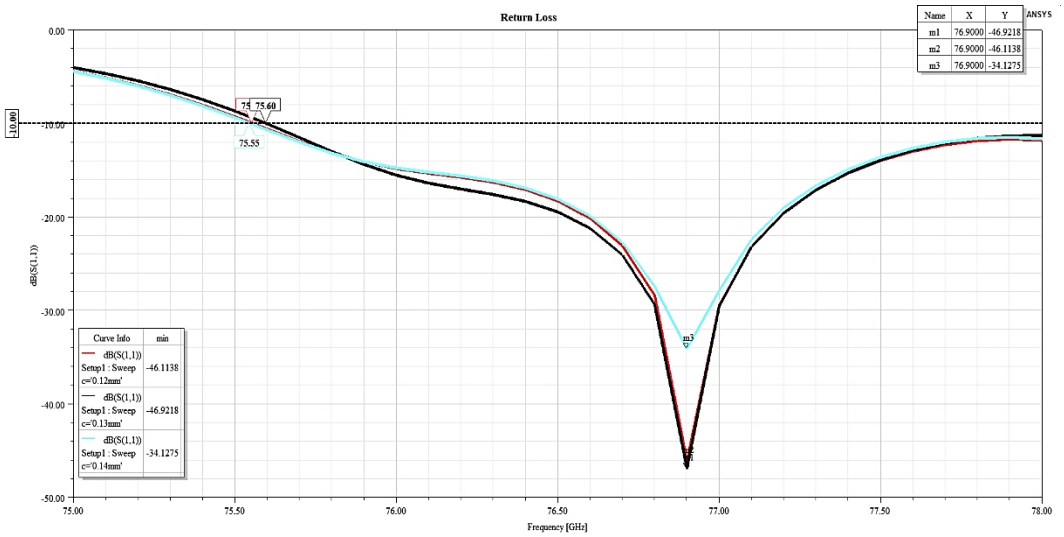

Figure 3.10: Return loss of varying tapered transmission line length (L_{TAPER})

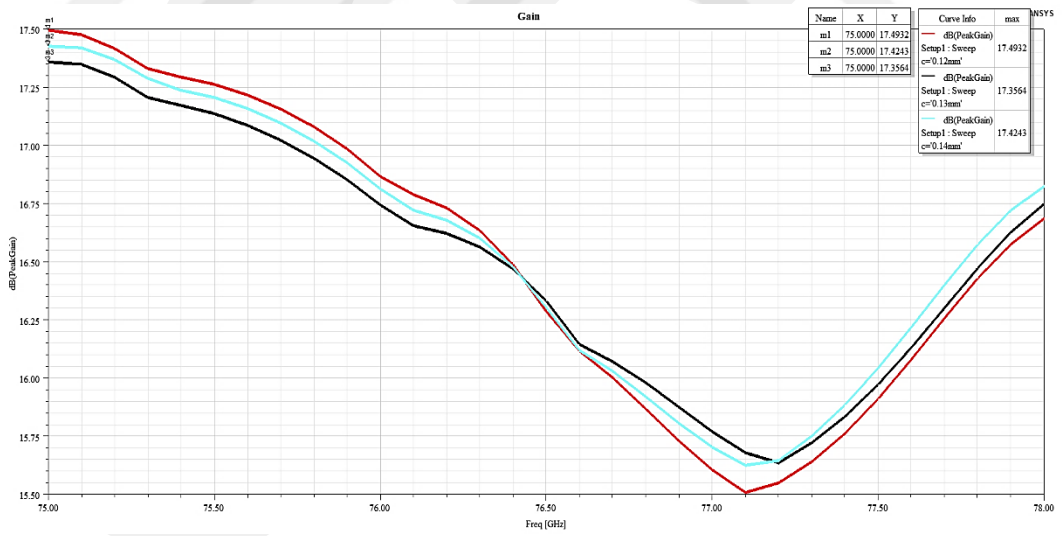

Figure 3.11: Gain versus frequency of varying tapered transmission line length (L_{TAPER})

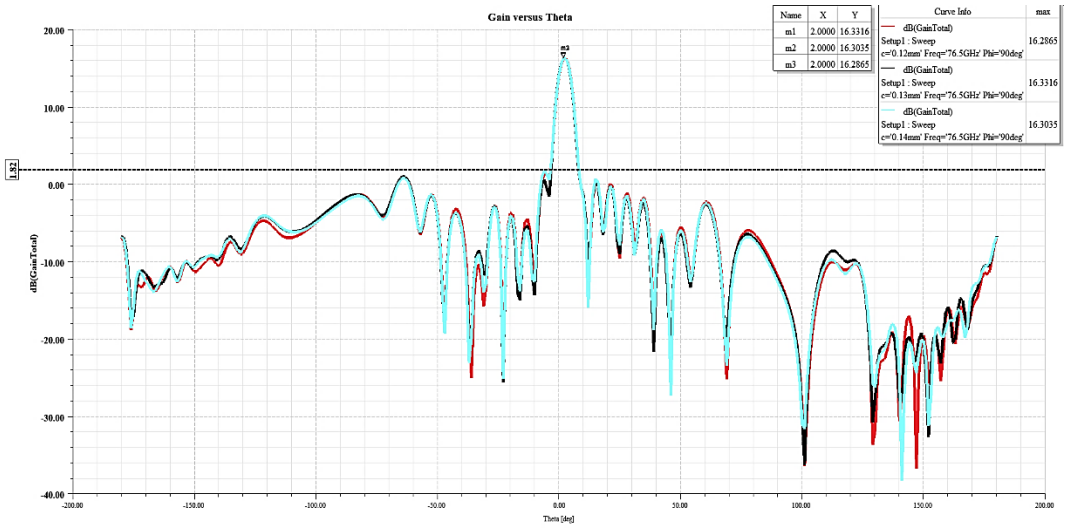

Figure 3.12: Gain versus theta of varying tapered transmission line length (L_{TAPER}) in elevation (y-z plane) and at 76.5 GHz

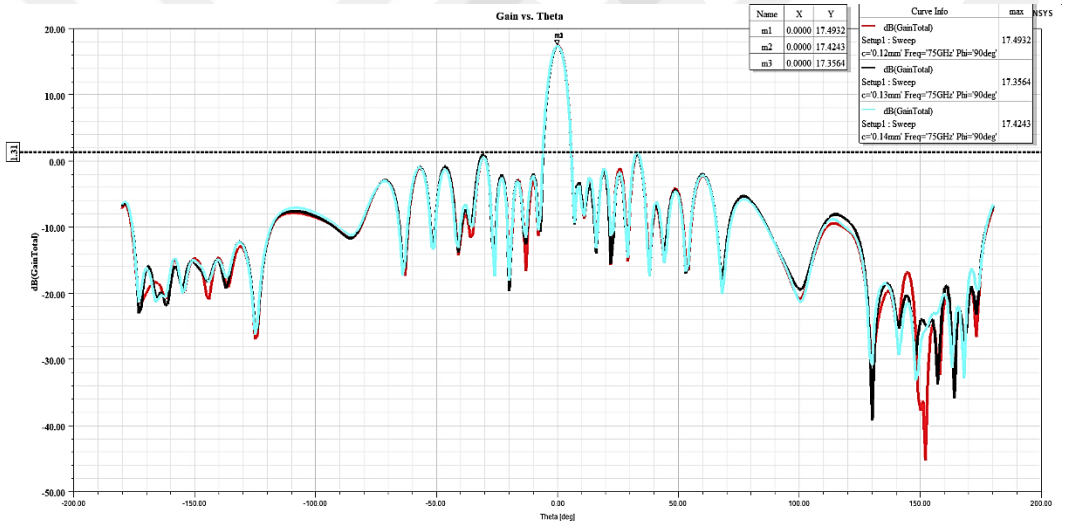

Figure 3.13: Gain versus theta of varying tapered transmission line length (L_{TAPER}) in elevation (y-z plane) and at 75 GHz

Figure 3.14: Normalized gain versus theta of tapered transmission line length (L_{TAPER}) in elevation (y-z plane) and at 76.5 GHz

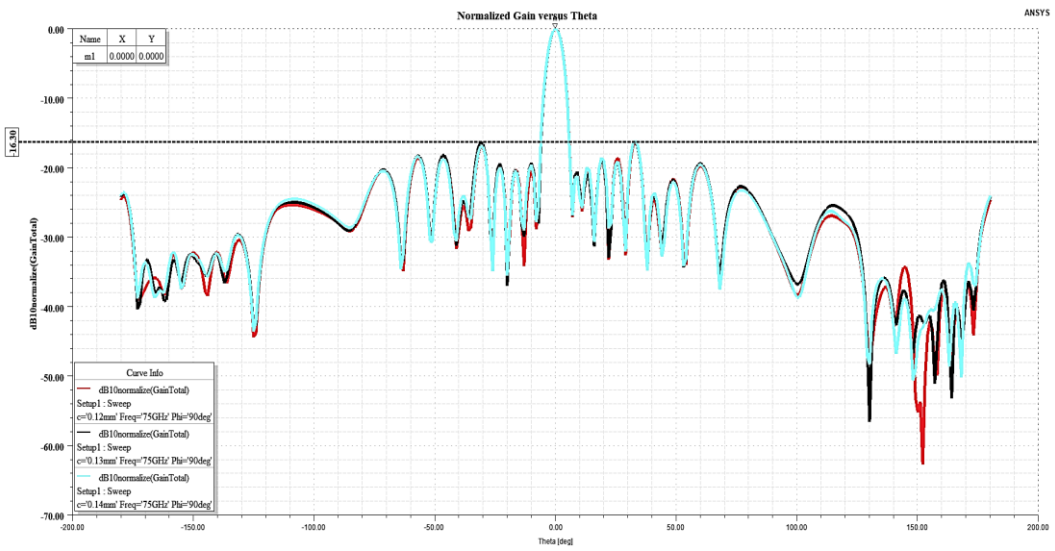

Figure 3.15: Normalized gain versus theta of tapered transmission line length (L_{TAPER}) in elevation (y-z plane) and at 75 GHz

While designing linearly tapered transmission line as a means of phased array, the most crucial point is that its length should be chosen exactly as an odd multiple of quarter guided wavelength (λ_g) to ensure that the array is in phase [45]. In addition, due to the lossy nature of transmission line, it is expected that as its length is extended the gain falls off. Therefore, its length should be determined precisely as an odd multiple of the calculated wavelength in dielectric substrate, meanwhile, it should be conserved as short as possible to avoid gain reduction. From the return loss graph in Figure 3.10 it is seen that, the variation of the length affects the reflection coefficient, and the antenna resonates at 76.9 GHz with the return loss falling below -46.9 dB in the best case. Quite a wide 10-dB impedance bandwidth of approximately 2.5 GHz is obtained from 75.55 GHz to 78 GHz. The gain-frequency graph in Figure 3.11 clearly shows that as the line length is increased the peak gain drops. Also, the normalized gain-theta graph at 76.5 GHz shows 2° shift in theta, whereas the pattern is seen to be accurately centered at 0° in theta at 75 GHz in the elevation plane (y-z). A maximum gain of about 17.49 dBi is accomplished at this stage with SLL standing below -14.51 dB at 76.5 GHz and, -16.3 dB at 75 GHz.

The last part of this stage deals with the ground pad width optimization as presented in the following simulation results.

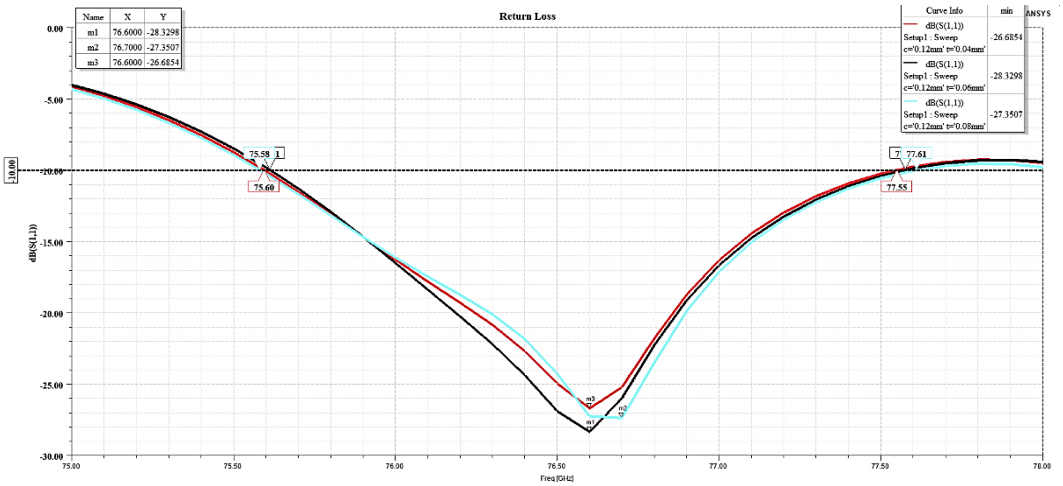

Figure 3.16: Return loss of varying ground pad width ($W_{GROUNDPAD}$)

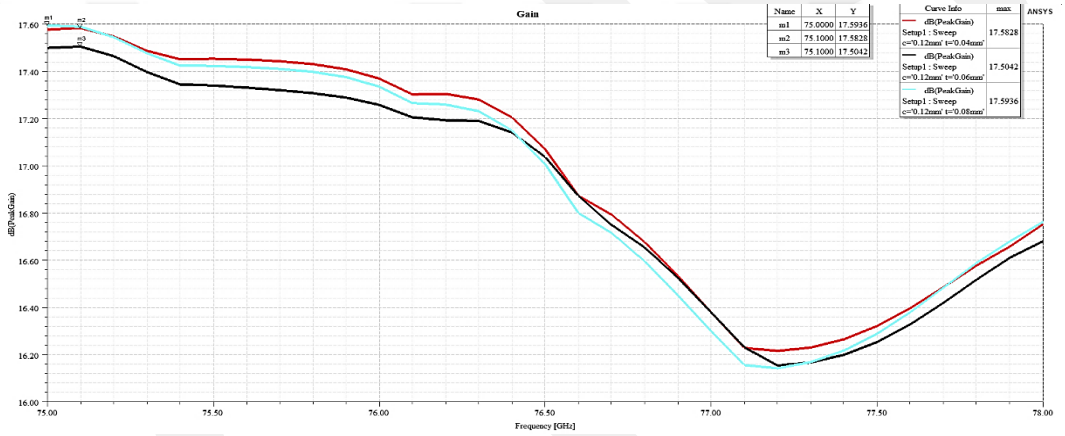

Figure 3.17: Gain versus frequency of varying ground pad width ($W_{GROUNDPAD}$)

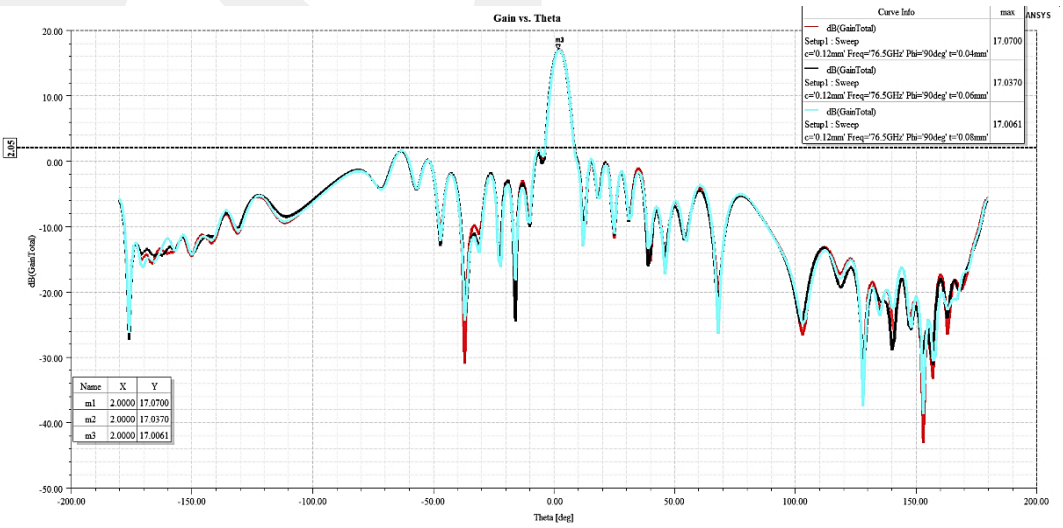

Figure 3.18: Gain vs. theta of varying ground pad width ($W_{GROUNDPAD}$) in elevation (y-z plane) at 76.5 GHz

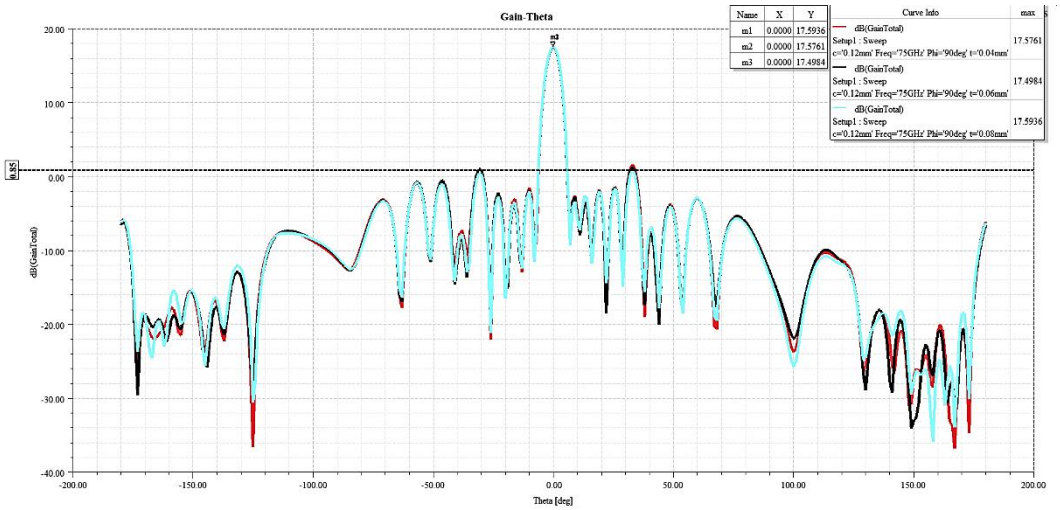

Figure 3.19: Gain vs. theta of varying ground pad width ($W_{GROUNDPAD}$) in elevation (y-z plane) at 75 GHz

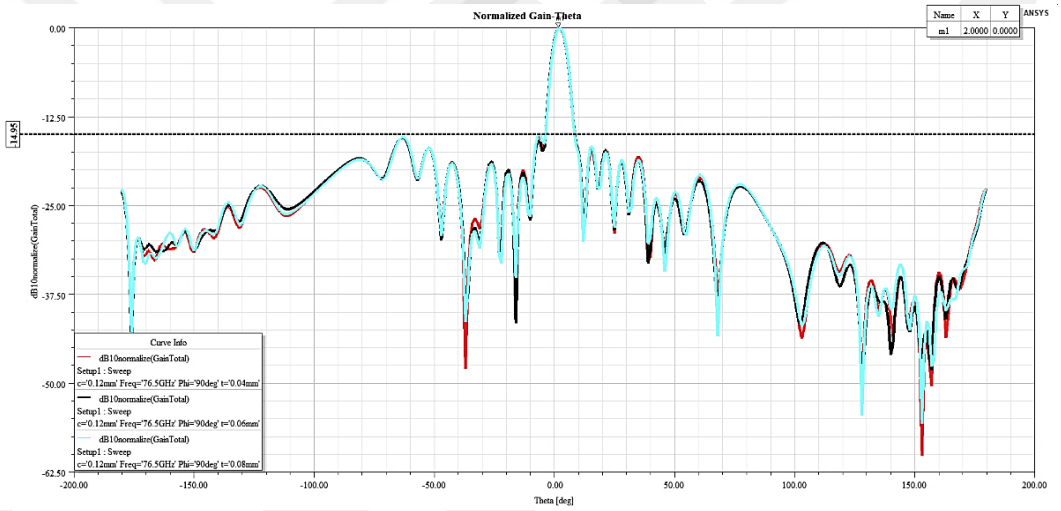

Figure 3.20: Normalized gain versus theta of ground pad width ($W_{GROUNDPAD}$) in elevation (y-z plane) and at 76.5 GHz

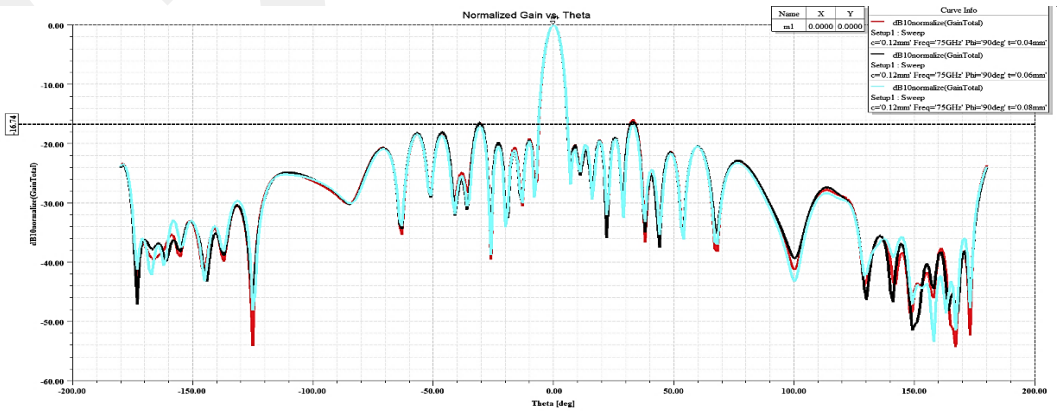

Figure 3.21: Normalized gain versus theta of ground pad width ($W_{GROUNDPAD}$) in elevation (y-z plane) and at 75 GHz

When working at mmWave band on-wafer waveguide probe feed is essential to excite the antenna, and GSG configuration is a common approach, however, this setup tends to excite parasitic modes. Ground pad width has a drastic effect on the suppression of parasitic higher order modes if chosen correctly. Referring to the attenuation constant, which is the real part of propagation constant, the phase constant, the imaginary part of the propagation constant and, also the steadiness of effective permittivity throughout the operating band reveals the unwanted multimode excitation. From the published investigations it is known that reducing the ground pad width helps prevent the higher order mode propagation [46-48]. On the other side, too narrow ground pad width is proven to be the main cause of additional parasitic effects due to field discontinuities of the probe to coplanar pad transition to the detriment of the calibrated measurement accuracy [46-48]. In addition, as a result of the simulation results above, it is observed that variation in ground pad width affects the location of resonance frequency and bandwidth. From Figure 3.17 it is observed that the gain is significantly enhanced as a result of ground pad width optimization, reaching up to a maximum of 17.59 dBi. Normalized gain plots in Figure 3.20 and 3.21 exhibit SLL of -14.95 dB at 76.5 GHz and, -16.74 dB at 75 GHz is achieved, respectively.

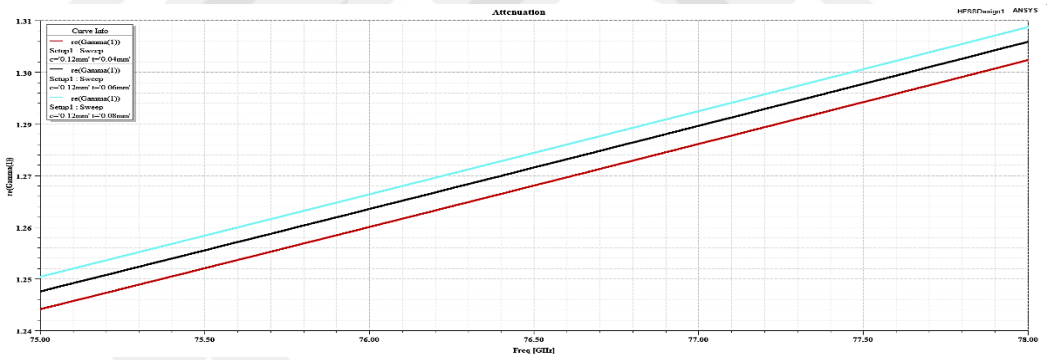

Figure 3.22: Attenuation constant (real part of propagation constant) versus frequency of varying ground pad width ($W_{GROUNDPAD}$)

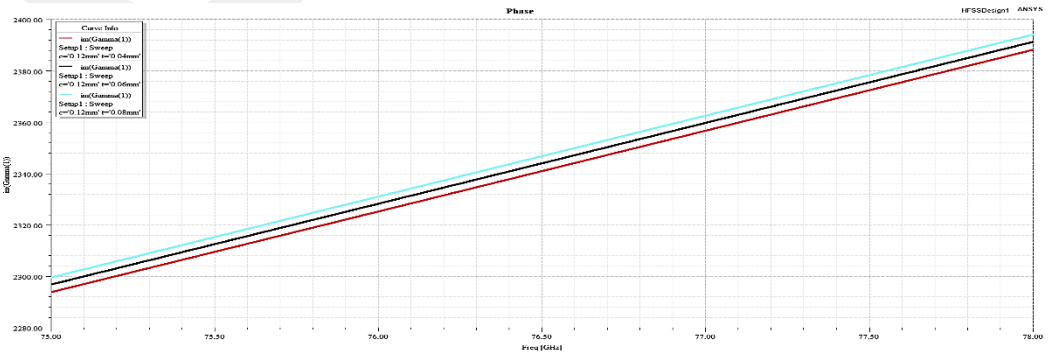

Figure 3.23: Phase constant (imaginary part of propagation constant) versus frequency of varying ground pad width ($W_{GROUNDPAD}$)

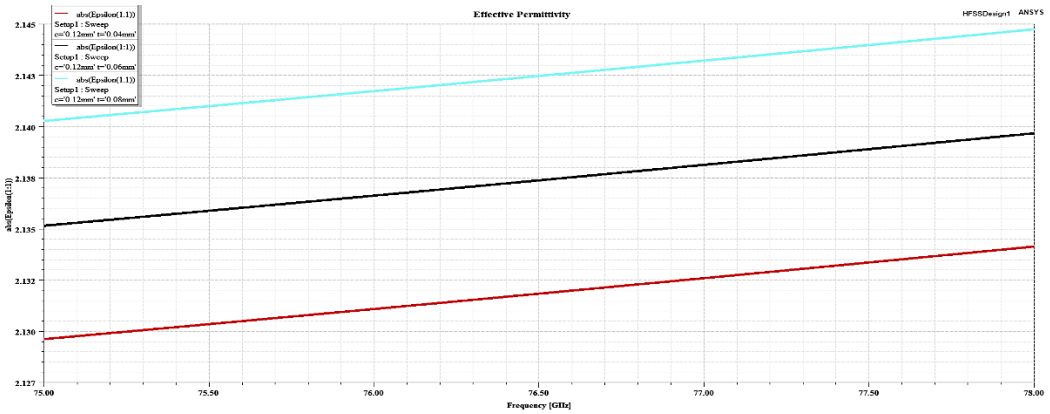

Figure 3.24: Effective Permittivity versus frequency with respect to varying ground pad width ($W_{GROUNDPAD}$)

From Figure 3.22, 3.23 and 3.24 propagation constant and effective permittivity graphs obviously show that there appears no higher order or additional undesired mode excitation for the specified ground pad widths. All the graphs exhibit a steady state linear upward trend. To sum up the above results related to determining the ground pad width, a compromise should be reached to avoid higher order modes and the coplanar waveguide (CPW) probe discontinuity effects.

3.1.2 Shorting Via Loaded Design

The last stage of the 76.5 GHz antenna is on shorting via incorporation into GSG padding for gain enhancement as shown in the following geometric structure and simulation results.

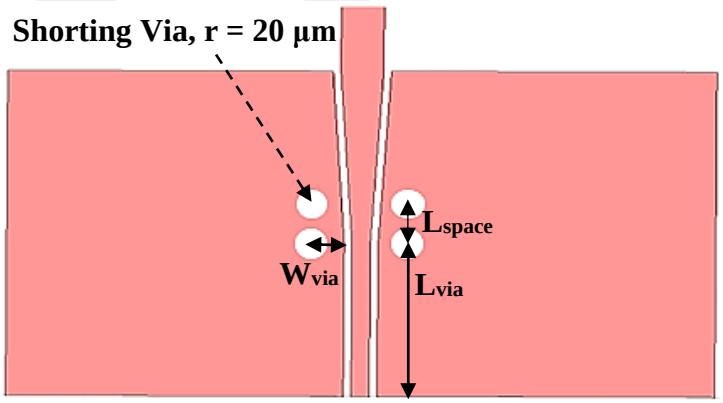

Figure 3.25: Top view geometry of shorting pin loaded GSG padding

Table 3.8: Dimensions of shorting pin positioning

L_{via}	L_{space}	W_{via}
1.48 mm	100 µm	80 µm

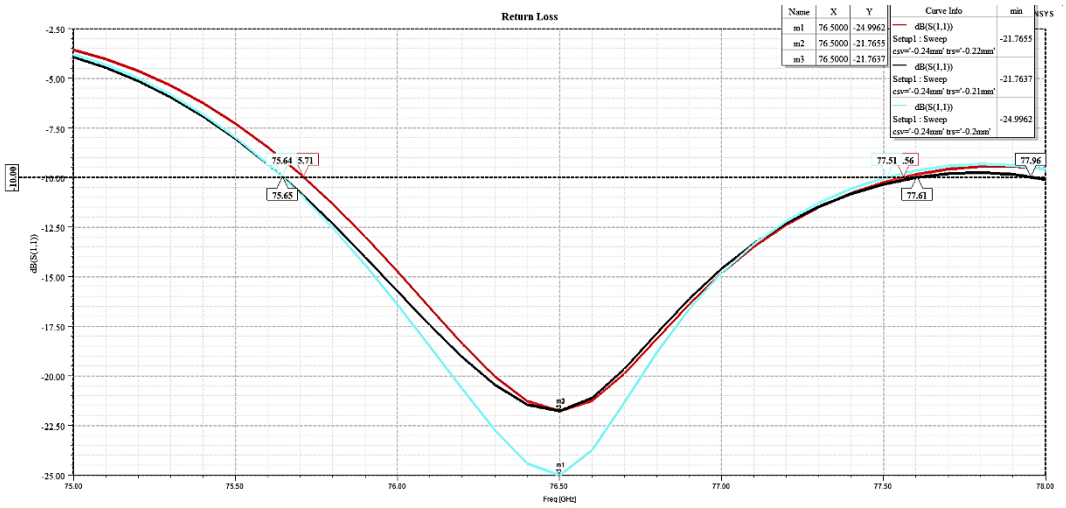

Figure 3.26: Return loss of varying shorting pin positioning (W_{via})

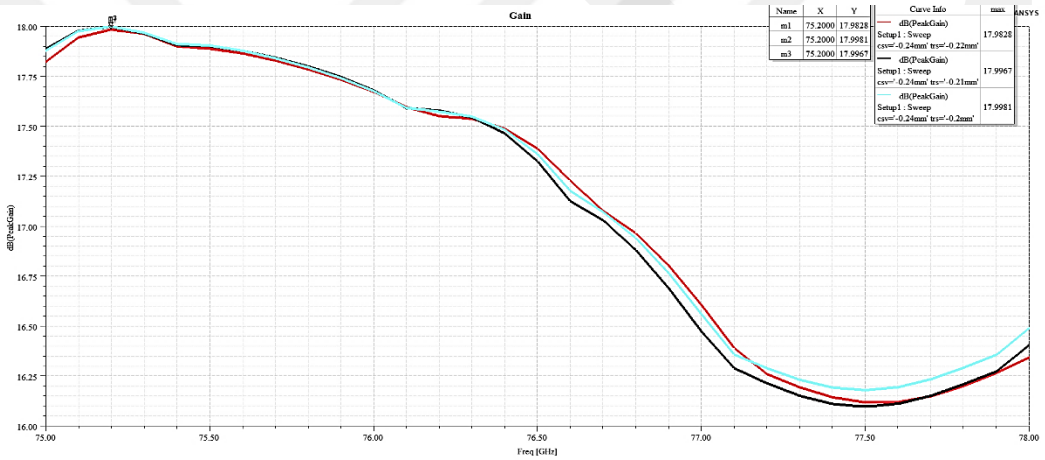

Figure 3.27: Gain versus frequency of varying shorting pin positioning (W_{via})

GSG padding is a commonly used mean, serving as a transition structure between waveguide microelectronic probe contacting transmission line and 50 Ω feed line connecting to radiating patch array. However, it is quite prone to parasitic higher order or evanescent modes [49]. These spurious modes are surface and slot-line modes, originating from discontinuities such as bends. In addition, GCPW transmission line has tendency to excite parallel plate mode (PPM). Hence, metallized vias are beneficial to avoid or to minimize the excitation of these parasitic modes if positioned accurately. In case of mispositioning of the vias, parallel plate mode can still propagate, particularly when the vias are spaced too far from each other [49]. Also, the vias should be placed as close as possible to the central signal trace to reduce the side metal channel, and via-to-via pitch should be less than $\lambda_g/4$ up to 100 GHz to prevent

undesired resonances [49]. Therefore, four shorting pins are positioned symmetrically to central signal trace and, positioning of the pins is optimized for gain improvement. Figure 3.26 and 3.27 show return loss and gain response to the distance variation of the vias to ground-signal spacing (W_{via}), respectively. Return loss graph demonstrates that the best impedance matching is achieved at -24.996 dB, when the vias' centers are placed 100 µm away from ground-signal gap. Figure 3.27 shows that 100 µm distancing yields higher peak gain at about 17.998 dBi and its minimum gain is higher than the other cases at above 16.2 dBi. It is also worth noting that it is observed that as the pin locations are moved further away outwards in the opposite direction of center signal trace the bandwidth deteriorates significantly. Thus, the pins should be positioned as close as possible towards the signal trace to avoid bandwidth reduction. The below graphs analyze via-to-via (V2V) separation.

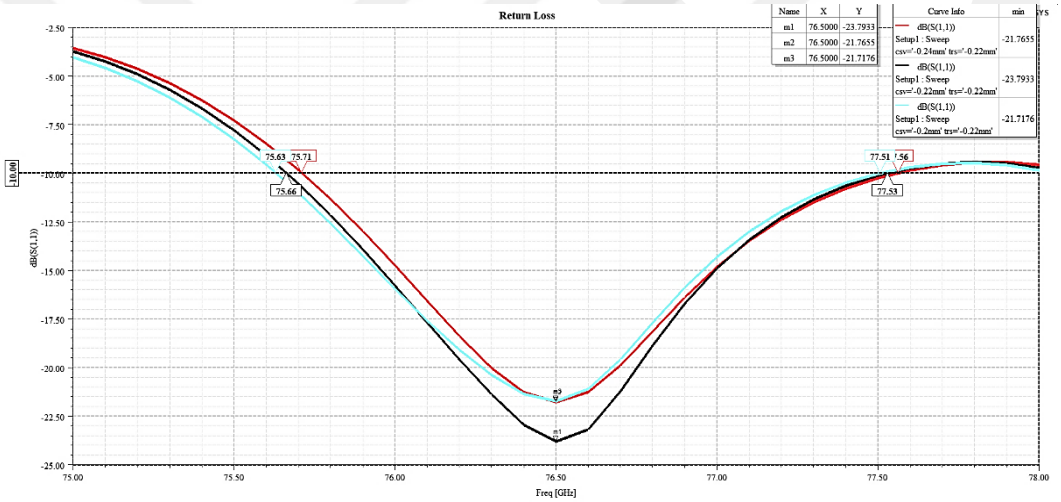

Figure 3.28: Return loss versus frequency of V2V separation variations

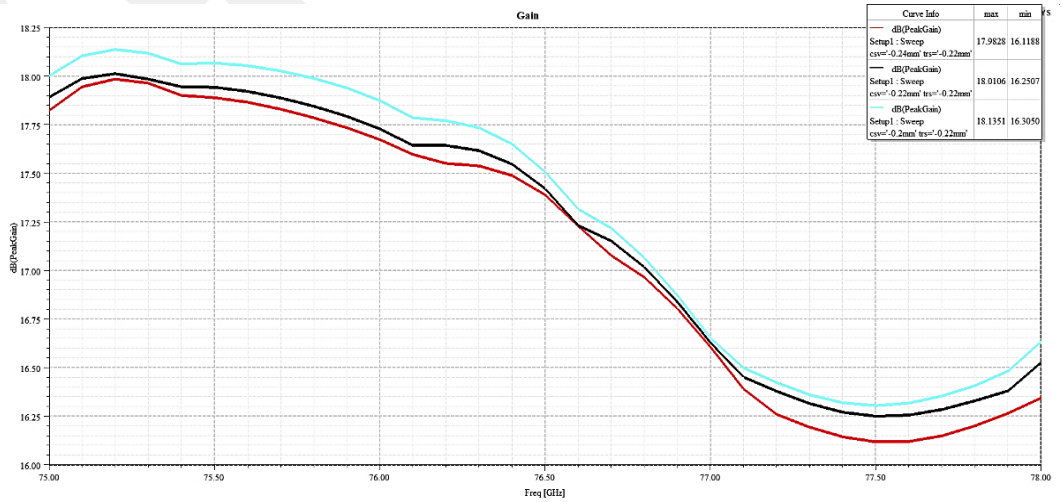

Figure 3.29: Gain versus frequency of V2V separation variations

Recalling from Fig. 3.25 that the via radius is r = 20 μm, the via spacing is varied from 1r to 3r in steps of 20 μm (r) and in this regard return loss and gain results are shown in Fig. 3.28 and 3.29, respectively. The limit of 20 μm is determined according to the technology restrictions, the possibility of damaging the wafer gets much higher when positioning via holes nearer than 20 μm. Looking at reflection coefficient graph in Fig. 3.28, the best impedance matching is provided by 1×r spacing at -23.973 dB, however the largest bandwidth of 1.88 GHz is given by 3×r spacing from 75.63 GHz to 77.51 GHz. Referring to gain graph in Fig. 3.29, the highest gain is clearly given by 3×r spacing reaching a peak value of above 18.135 dBi, and its minimum is at 16.305 dBi, exhibiting a maximum fluctuation of 1.83 dBi throughout the whole operating band.

3.1.3 Comparative Analysis Between Vialess and Via Loaded Designs

To conclude this stage, 76.5 GHz linear array antenna design, the end performance results of without shorting pin and with shorting pin are compared below for clarity.

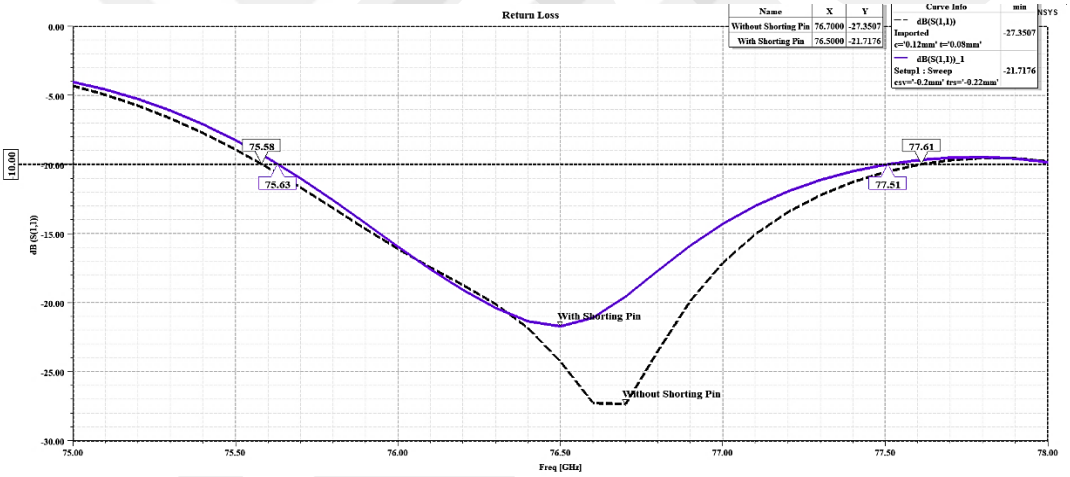

Figure 3.30: Reflection coefficient versus frequency

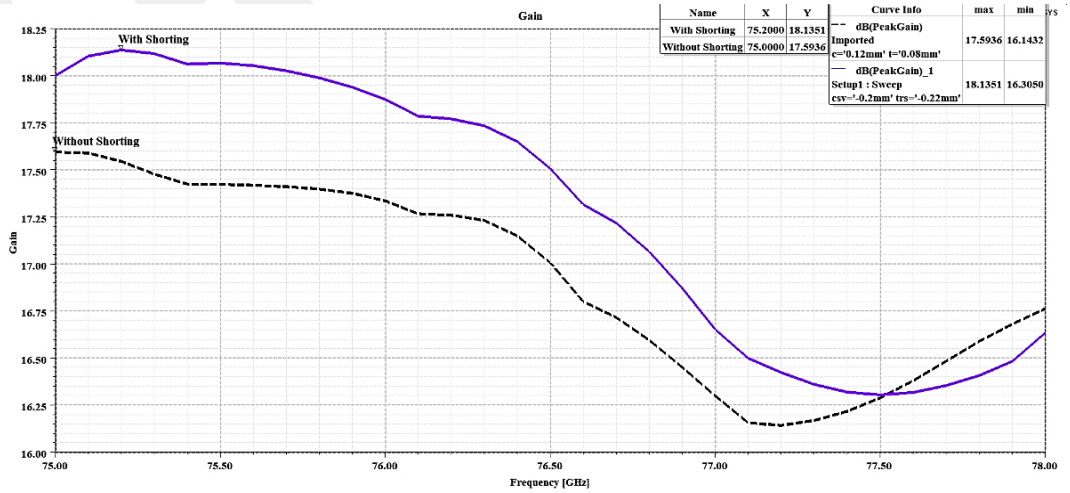

Figure 3.31: Gain versus frequency

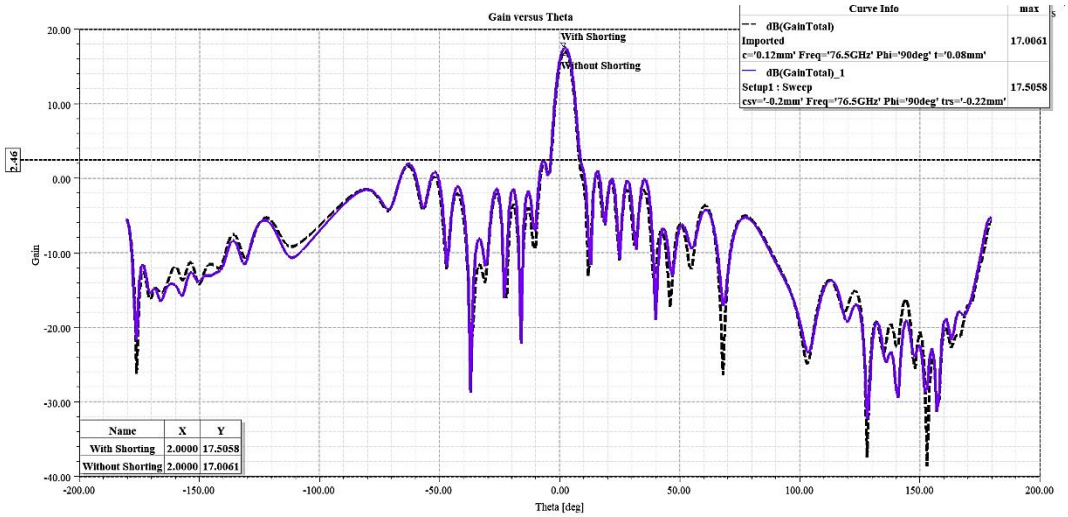

Figure 3.32: Gain versus theta (at phi = 90°) in E-plane (y-z plane) at 76.5 GHz

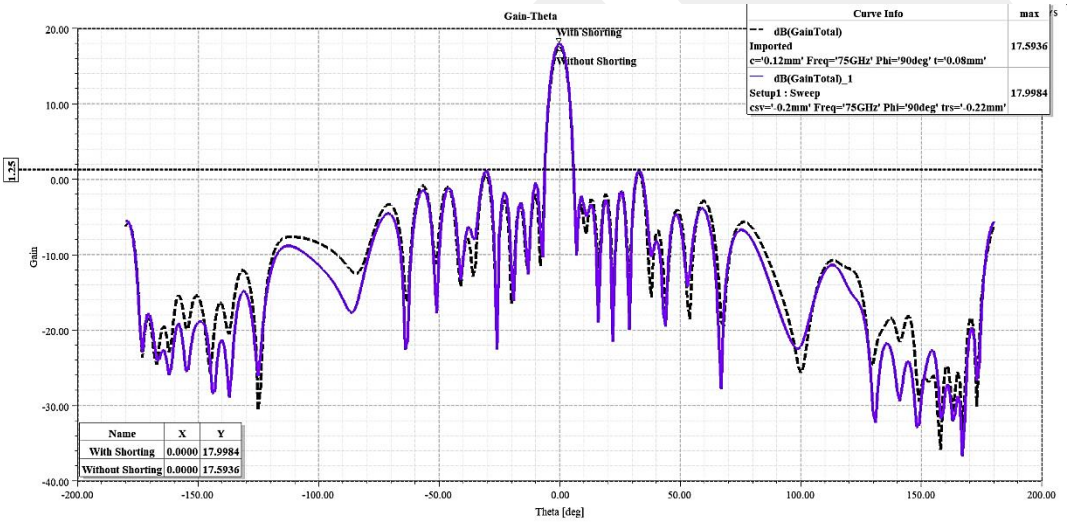

Figure 3.33: Gain versus theta (at phi = 90°) in E-plane (y-z plane) at 75 GHz

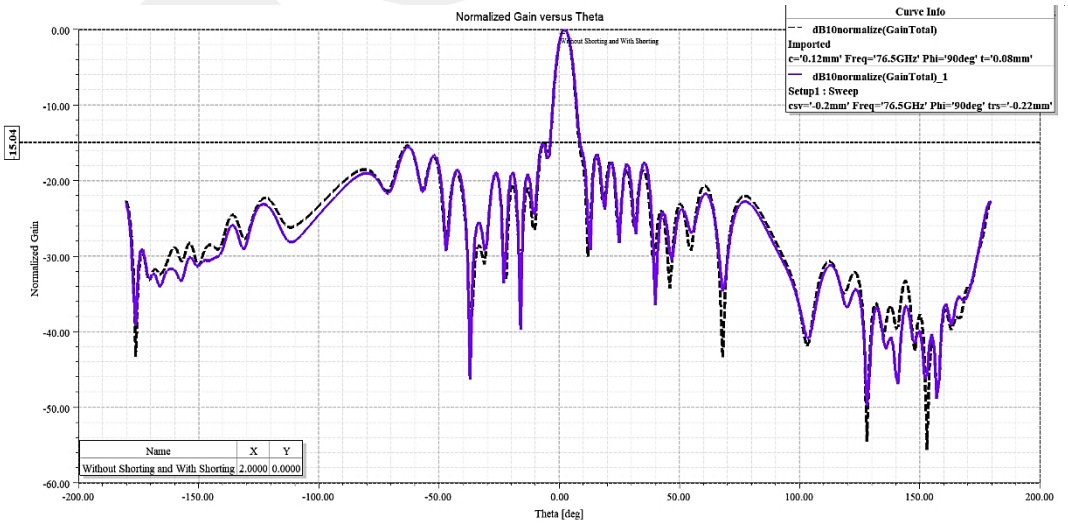

Figure 3.34: Normalized gain vs. theta (at phi =90°), E-plane (y-z plane) at 76.5 GHz

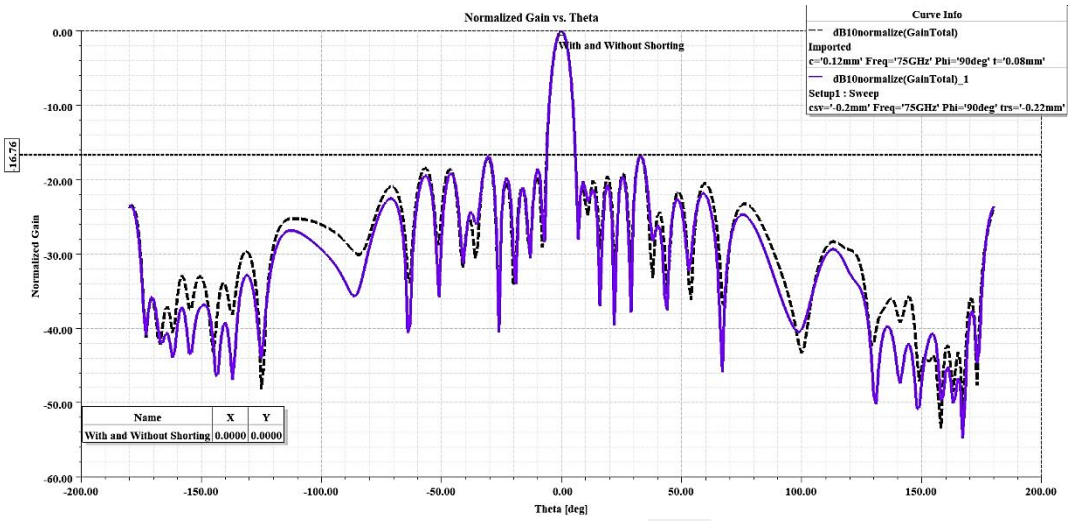

Figure 3.35: Normalized gain vs. theta (at phi = 90°), E-plane (y-z plane) at 75 GHz

Looking at Fig 3.30, return loss graph obviously shows that shorting via loaded design exhibits a poorer impedance matching with return loss of -21.7176 dB than vialess design with return loss of -27.3507 dB. When the resonance frequencies are assessed, vialess case shows a 200 MHz shift from the excitation frequency at 76.7 GHz, while the via loaded case can resonate at 76.5 GHz without any shift. Subsequently to loading vias to the antenna, the bandwidth shows a shrink from 2.03 GHz (vialess case) to 1.88 GHz (with vias case). At the vialess stage, it possesses a -10 dB bandwidth from 75.58 GHz to 77.61 GHz, fulfilling the targeted band interval, which is implemented in the reference [15]. Via loading to GSG transition structure is shown to have a detrimental effect on the -10 dB bandwidth resulting from 75.63 GHz to 77.51 GHz in Fig. 3.30.

Fig. 3.31 represents the peak gain with respect to the operating frequency. Shorting pin loaded case has drastically higher gain in comparison to the pinless case throughout the entire band, except for 77.5-78 GHz interval, which is out of scope at this stage. The average gain is improved by 0.375 dB thanks to shorting via loading. And the maximum peak gain rises to 18.1351 dB from 17.5936 dB after incorporation of shorting vias. It is also noteworthy that minimum gain grows from 16.1432 dB to 16.305 dB with the aid of shorting via inclusion. The general downward trend in gain especially for 76.5 GHz and the above frequencies can be attributed to increasing beam steering angle. As the angle of steer increases the antenna quality deteriorates because phased array antenna focuses worse at larger angles, resulting in a wider beamwidth. Fig. 3.32 and 3.33 show two-dimensional rectangular radiation pattern in E-plane at

76.5 GHz and 75 GHz, respectively. The maximum gain at 76.5 GHz pattern is at 17.01 dB for vialess case and at 17.5058 dB for via loaded case, resulting in a SLL of -14.55 dB (vialess) and -15.05 dB for via loaded design. When 75 GHz pattern is analyzed, the maximum gain is at 17.5936 dB for vialess case and it is 17.9984 for via included case, marking a SLL of -16.35 dB for no-via case and, of -16.75 dB for via loaded case.

Fig. 3.34 and 3.35 present normalized two-dimensional rectangular E-plane radiation pattern at 76.5 GHz and 75 GHz, respectively. From the 76.5 GHz pattern, it is seen that the SLL is at -15.04 dB, while at 75 GHz SLL is reduced to -16.76 dB. In addition, 2° shift in pattern is observed at 76.5 GHz, and 75 GHz the pattern is centered at 0°. Ideally, the 76.5 GHz pattern is expected to be centered at 0°. This slight shift can be attributed to the length of tapered line, and it is related to the port type used in the electromagnetics solver. Because its operational principles resemble the waveguide behavior, waveport is employed in HFSS simulations in this work, however, vertical metallized bridge excitation technique can be employed with lumped port as another available option.

For all the radiation pattern simulations the emphasis is put on E-plane behavior corresponding to y-z plane in elevation and at phi = 90°, because all the array elements are aligned along y-axis. Therefore, the designed antenna exhibits radiation characteristic similar to end-fire array with its E-plane being normal to the plane of patch (z-axis direction) and in the direction of all the array elements are concatenated in series (y-axis direction) (from end to end).

To summarize this stage, at the beginning, free space wavelength, guided wavelength, dimensions of patch, effective substrate permittivity, resonance frequency and fringe factor are calculated theoretically using transmission line model analysis. At the next step, patch antenna array is designed in HFSS referring to the dimensions in reference article [15]. Because of that GSG padding dimensions were lacking in the article, all the related dimensions are optimized (transmission line length, tapered line length and ground pad width) respectively. As a result, the optimum dimensions are determined in terms of the bandwidth and peak gain. After that, four shorting metallized vias are loaded to GSG transition structure to enhance the gain and to suppress the spurious excitation modes. Consequently, the overall gain is observed to significantly increase.

The bandwidth and the reflection coefficient are observed to slightly deteriorate relatively to the vialess antenna.

3.2 Linear Patch Antenna Array Design at 79 GHz

At first, theoretical estimations are made for a single resonant rectangular patch element etched on RO3003 substrate of 0.127 mm (5 mil) thickness and with relative permittivity of ε_r = 3 at 79 GHz by using transmission line model, as preliminary findings demonstrated in the table below.

Table 3.9: Transmission-line model calculations of 79 GHz antenna

Parameters	Value
Width (mm)	1.3417
Effective Dielectric Constant	2.6842
Actual Length (mm)	1.0355
Effective Length (mm)	1.1581
Guided Wavelength (mm)	2.3162
Free Space Wavelength (mm)	3.7948
Resonance Frequency (MHz)	78,999,999.67
Fringe Factor ('q')	0.94523

3.2.1 Proposed Method to Adjust the Main Beam Steering

The excitation frequency is risen from 76.5 GHz to 79 GHz and, the targeted operating bandwidth is 77-81 GHz at this stage. Because of the rise in the operating frequency the guided wavelength decreases, thus the phase delay between each two successive array elements increases, resulting in larger steer angle of major lobe at center frequency. Therefore, the spacing between each two successive elements should be adjusted to center the main beam at 0° in E-plane at 79 GHz, the center frequency. Additionally, probable directivity loss can be avoided by setting the major lobe steer angle. To make this transformation, GSG dimensions are optimized initially as below.

Table 3.10: Renewed dimensions of GSG padding transition structure (Model 1)

L_{FEED}	L_{TAPER}	W_{GSG_SPACE}	W_{FEED}	$W_{GROUNDPAD}$
1.14 mm	1.68 mm	50 μm	0.12 mm	1.42 mm

Table 3.11: Renewed dimensions of GSG padding transition structure (Model 2)

L_{FEED}	L_{TAPER}	W_{GSG_SPACE}	W_{FEED}	$W_{GROUNDPAD}$
1.3 mm	1.5201 mm	40 µm	0.12 mm	1.72 mm

There are two models proposed for this stage and their comparative operational characteristics are demonstrated below.

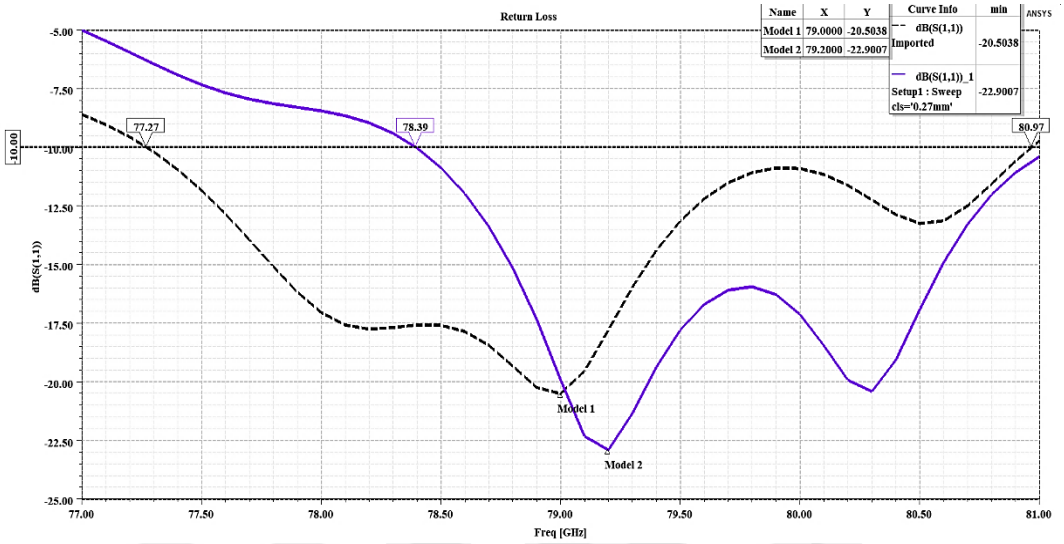

Figure 3.36: Reflection coefficient versus frequency (dB)

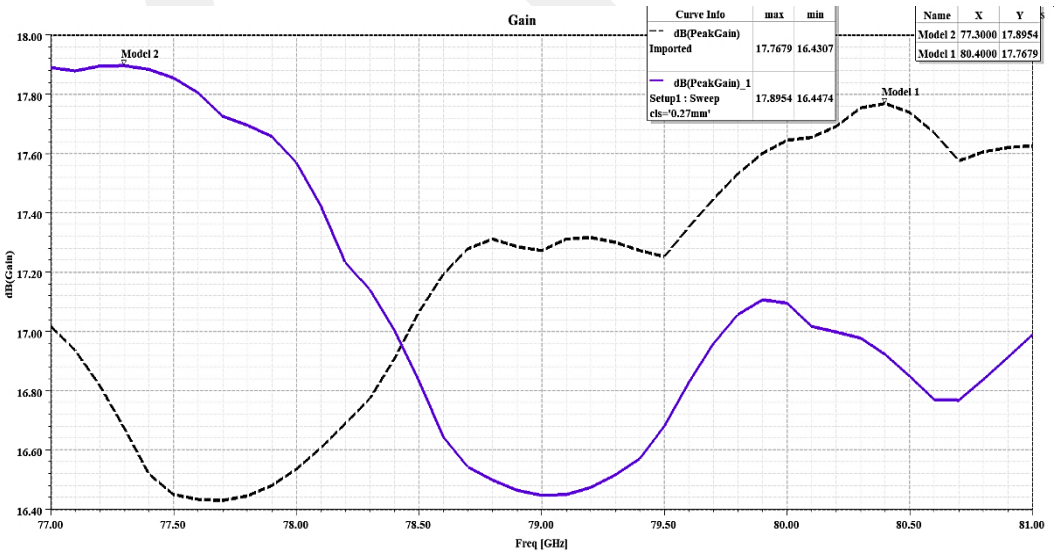

Figure 3.37: Gain versus frequency (dBi)

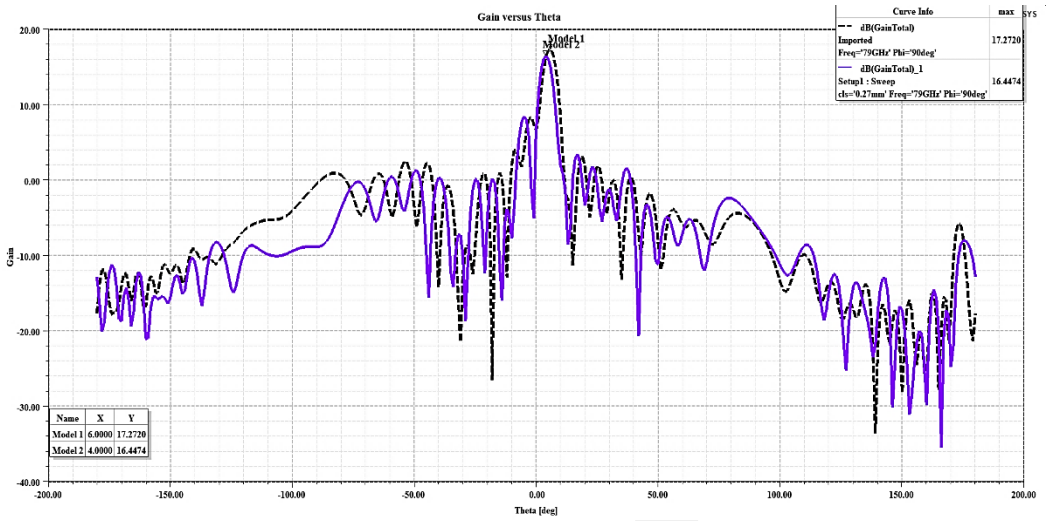

Figure 3.38: Gain versus theta (at phi = 90°) in E-plane (y-z plane) at 79 GHz

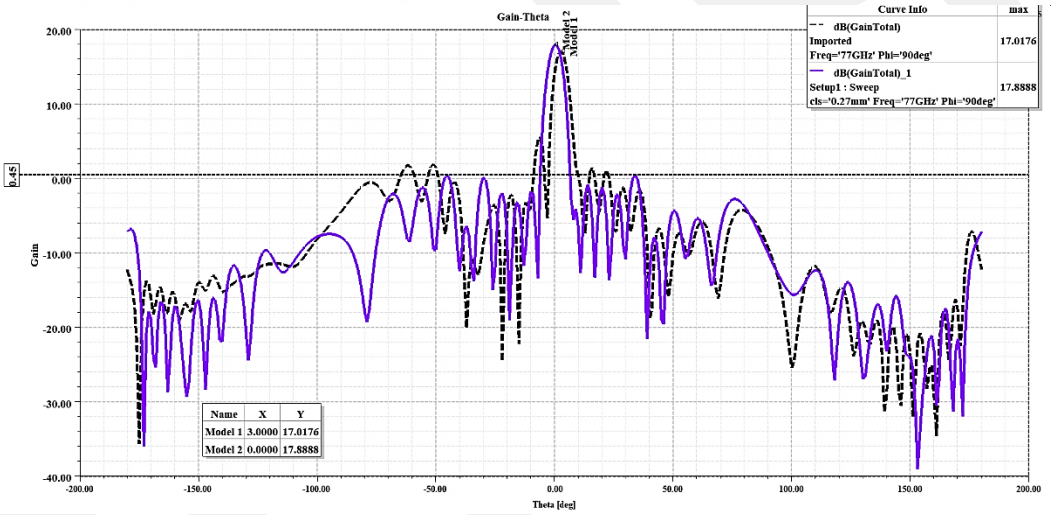

Figure 3.39: Gain versus theta (at phi = 90°) in E-plane (y-z plane) at 77 GHz

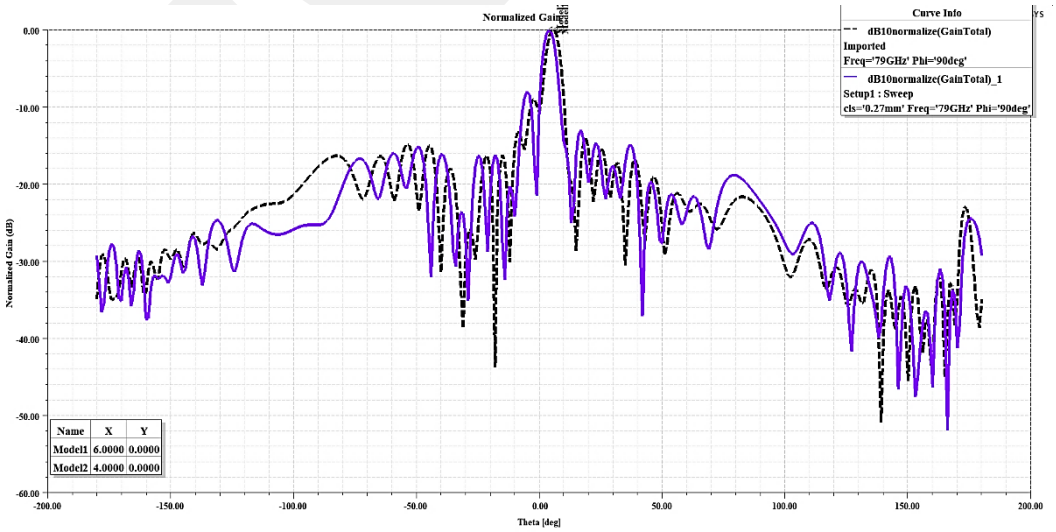

Figure 3.40: Normalized gain vs. theta (at phi=90°) in E-plane (y-z plane) at 79 GHz

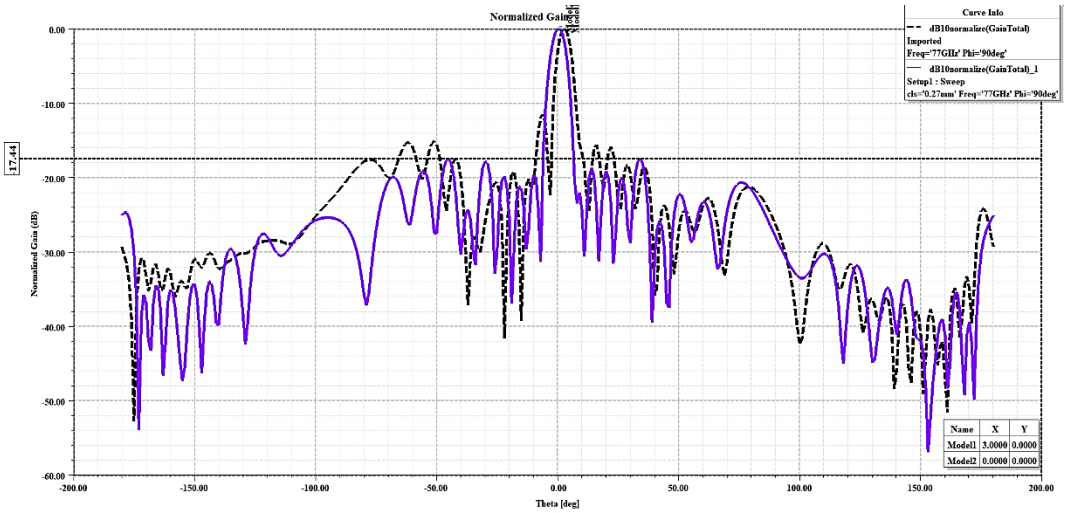

Figure 3.41: Normalized gain vs. theta (at phi=90°) in E-plane (y-z plane) at 77 GHz

Table 3.12: Calculated phase shift of each array element for Model 1

Ψ (1) = 17.96°	Ψ (5) = 89.51°	Ψ (9) = 156.86°	Ψ (13) = 223.92°
Ψ (2) = 35.34°	Ψ(6) = 106.17°	Ψ (10) = 173.515°	Ψ (14) = 242.75°
Ψ (3) = 53.45°	Ψ (7) = 123.55°	Ψ (11) = 190.896°	Ψ (15) = 260.13°
Ψ (4) = 71.41°	Ψ (8) = 140.93°	Ψ (12) = 206.54°	Ψ (16) = 277.51°

When designing Model 1, the length of all the array elements (L) is decreased to 1.07 mm because of the decreasing guided wavelength (λ_g) and GSG pad dimensions are set to the values in Table 3.10. After obtaining the performance results, total phase shift of each array element is calculated in Table 3.12 employing the formulae in 2.30.

During the design of Model 2, GSG pad dimensions are set to the values in Table 3.11. The emphasis is put on scaling all the spacings between each successive array element by a constant scale factor, which is calculated as “0.98” because of the decreasing operating guided wavelength (λ_g). In addition, the length of all the array elements (L) is scaled by “0.98” according to the actual length value calculated in Table 3.9 using transmission line model. Also, the length of quarter wave transformer stub (L_{STUB}) is scaled by the factor “0.98”. And the tapered transmission line length (L_{TAPER}) is set to the exactly three times the length of quarter wave impedance transformer to ensure that the array is in phase. The scaling operation is applied to prevent undesired main beam steering due to the decreased wavelength, in other words to keep the array in phase. The detriment to antenna quality or directivity is avoided as well utilizing the

scale method.

Two designs are simulated in HFSS to observe the consequences of this method. Fig. 3.36 compares the return loss. Model 1 exhibits a larger bandwidth compared to Model 2 (scaling applied). This phenomenon can be probably related to reduced conducting cross section area of patch array elements, because Model 2 employs smaller (scaled) patch length (L). Therefore, smaller patch elements lead to narrower bandwidth. While Model 2 possesses lower resonance return loss than Model 1 with -22.9007 dB at 79.2 GHz and -20.5038 at 79 GHz, respectively.

Fig. 3.37 refers to gain with respect to the operating frequency. Model 2 provides better overall gain, reaching up to 17.8954 dBi at 77.3 GHz, whereas Model 1 gives 17.7679 dBi at 80.4 GHz. Additionally, minimum gain of Model 2 is slightly higher than Model 1 of about 0.017 dBi.

Fig. 38 and 39 evaluates the total gain regarding the angle theta (θ) at 79 GHz and 77 GHz, respectively. These graphs as well as Fig. 3.40 and 3.41 signify substantial decline in the angle of main lobe steering at center frequency (79 GHz) and at 77 GHz. Applying the scale method (Model 2) produce remarkably better results in terms of steer angle correction when compared to unscaled Model 1. Fig. 38 and 3.40 shows 2° correction at 79 GHz, the center frequency, but the unscaled design interestingly focuses better with 17.27 dBi than the scaled design having 16.45 dBi.

Fig. 39 and 3.41 (normalized) show total gain pattern at 77 GHz. 3° correction is accomplished consequently to performing scale method, thus centering Model 2 at 0° with SLL of -17.44 dB in E-plane.

To sum up, two antennas are designed for the target interval of 77-81 GHz at this stage. Model 1 fulfills the operational requirements in terms of -10 dB bandwidth, however, at the expense of 6° main beam steer angle at center frequency. Therefore, a method is proposed based on scaling all the spacing distances between consecutive array elements to fine tune the phase delays. 2° steer angle correction is implemented at center frequency (79 GHz) and 3° steer angle correction is achieved at 77 GHz radiation pattern by virtue of this proposed method.

CHAPTER 4

CONCLUSION

This thesis focuses on beam scanning series fed phased array composed of sixteen linearly concatenated patch elements through operating frequency variation. The aimed frequency interval is 75.6-77.5 GHz at the first stage, and 77-81 GHz at the second stage. In addition, pencil beam with high directivity is targeted for compatibility with medium and long-range automotive radar. For this purpose, single layered microstrip patch antenna array is proposed with an optimized waveguide to microstrip line transition structure.

Initially, theoretical background information on microstrip patch antenna, scanning phased array theory and Chebyshev weighting array is provided comprehensively. Subsequently, 16 element patch array is designed by using Chebyshev distribution for SLL reduction. After that, a transition structure is designed to enable the on-wafer GSG probe contact between the waveguide probe and microstrip feed line connecting to radiating patch. A series of simulations are performed as parametric study to optimize GSG padding dimensions, which are the input feed line and tapered transmission line length and also ground pad width. Performance characteristics are evaluated based on theoretical background. In the next step, the effect of shorting pin loading to ground pads of GSG transition is investigated in detail. From the parametric simulations in terms of shorting pin positioning and its radius, it is observed that incorporating shorting pin to GSG pads significantly contributes to directivity and gain. However, it can cause slight bandwidth reduction. Moreover, its capability of spurious excitation mode suppression is highlighted if positioned accurately. As a result, 75.63-77.51 GHz -10 dB bandwidth with maximum gain of above 18.1 dBi and with SLL of below -15 dB at center frequency (76.5 GHz) is accomplished. Additionally, comparative analysis between vialess and via loaded cases is conducted.

At the second stage, the targeted spectrum range is 77-81 GHz and for this purpose

two design models are proposed. Hence, GSG dimensions are optimized in accordance with the new band. This model worked in the interval of 77.27-80.97 GHz referring to the related -10 dB return loss. However, 6° main beam steer is observed at center frequency. For centering main lobe to 0° a method is proposed based on scaling the spacing distances between consecutive array elements to fine tune the phase delay. As a result of implementing the scaling operation not only on spacings but also on the length of array elements, Model 2 is produced with -10 dB bandwidth at 78.39 -81 GHz. Its gain reached up to 17.895 dBi. And main beam steer is corrected from 6° to 4° at 79 GHz center frequency. Furthermore, it is corrected from 3° to 0° at 77 GHz by virtue of this proposed method.

Frequency dependent beam scanning microstrip antenna is commonly preferred in the automotive industry, for long range adaptive cruise control radar module in particular. However, undesired beam steer correction still remains challenging. Also, bandwidth and gain enhancements are still needed because this type of linear array is limited only to a few GHz. Consequently, advanced phase correcting techniques can be developed to provide a more precise control of the phased array steer angle for future research endeavors.

REFERENCES

[1] C. A. Balanis, *Antenna Theory: Analysis and Design*. John Wiley and Sons, 2016.

[2] N. Almuqati, H. Sigmarsson, "3d microstrip line taper on ultra-low dielectric constant substrate,", *IEEE 20th Wireless and Microwave Technology Conference*, USA, 2019.

[3] P. Ranjan, "A new approach for improving the bandwidth of microstrip patch antenna,", *2nd International Conference on Micro-Electronics and Telecommunication Engineering*, 2018.

[4] S. Liu, W. Wu, D. G. Fang, "Wideband monopole-like radiation pattern circular patch antenna with high gain and low cross-polarization,", *IEEE Transactions on Antennas and Propagation*, vol. 64, no. 5, pp. 2042 – 2045, 2016.

[5] W. A. Awan, "Very small form factor with ultra-wide band rectangular patch antenna for 5G applications,", *International Conference on Computing, Mathematics and Engineering Technologies*, 2018.

[6] W. A. Awan, A. Zaidi, N. Hussain, A. Baghdad, "Compact size Y-shaped broadband antenna for E-band applications," *International Conference on Wireless Technologies, Embedded and Intelligent Systems*, 2019.

[7] N. M. Rashad, A. L. Hussesin, A. A. M. Khalaf, "Two-element pharaonic ankh-key array antenna design, simulation, and fabrication for 5G and millimeter-wave broadband applications.", *IEEE Access*, vol. 10, pp. 15175 – 15182, 2022.

[8] J. A. Oladapo, Z. Yunusa, D. S. Shuaibu, M. N. Hamidon, "E-band slotted microstrip patch antenna array for 5G broadband applications,", *2nd International Conference on Telematics and Future Generation Networks*, 2018.

[9] H. Chen, Y. Shao, Y. Zhang, C. Zhang, Z. Zhang, "A low profile broadband circularly polarized mmWave antenna with special-shaped ring slot.", *IEEE Antennas and Wireless Propagation Letters*, vol. 18, no. 7, pp. 1492 – 1496, 2019.

[10] A. Sain, K. L. Melde, "Impact of ground via placement in grounded coplanar waveguide interconnects.", *IEEE Transactions on Components, Packaging and Manufacturing Technology*, vol. 6, no. 1, pp. 136 – 144, 2016.

[11] Y. Shen, H. Zhang, Y. Luo, “A miniaturized mmWave antenna based on zero mode,”, *13th International Symposium on Antennas, Propagation and EM Theory,* China, 2021.

[12] P. K. Desai, B. Neelgar, “Design of compact 4x4 MIMO antenna with dgs structure for 5G mmWave communication,”, International Conference on Circuits, Controls and Communications, 2021.

[13] S. Soti, P. K. Chakravarti, “A compact patch antenna with dgs for 28 GHz 5G millimeter band applications,”, IEEE 7th International Conference for Convergence in Technology, 2022.

[14] M. F. Nakmouche, D. E. Fawzy, A. M. M. A. Allam, H. Taher, M. F. A. Sree, “Dual band siw patch antenna based on h-slotted dgs for Ku band applications,”, 7th International Conference on Electrical and Electronics Engineering, 2020.

[15] J. Yan, H. Wang, J. Yin, C. Yu, W. Hong, “Planar series-fed antenna array for 77 GHz automotive radar,”, Sixth Asia-Pacific Conference on Antennas and Propagation (APCAP), 2017.

[16] B. Jian, J. Yuan, Q. Liu, “Procedure to design a series-fed microstrip patch antenna array for 77 GHz automotive radar,”, Cross Strait Quad-Regional Radio Science and Wireless Technology Conference, 2019.

[17] N. Ram, G. Hongmin, M. S. Sadiq, A. C. Bahadur, “77 GHz corporate feed series microstrip antenna array for the applications of automotive radar,” Ninth Asia-Pacific Conference on Antennas and Propagation, 2020.

[18] W. Wei, X. Wang, “A 77 GHz series-fed weighted antenna arrays with suppressed side-lobes in E- and H-planes.”, Progress in Electromagnetics Research Letters, vol. 72, pp. 23-28, 2018.

[19] J. Xu, W. Hong, H. Zhang, G. Wang, Y. Yu, Z. H. Jiang, “An array antenna for both long- and medium-range 77 GHz automotive radar applications.”, IEEE Transactions on Antennas and Propagation, vol. 65, no. 12, pp. 7207-7216, 2017.

[20] X. Shang, F. S. Zhang, R. He, H. J. Zhang, “A 77 GHz miniaturized microstrip antenna array for automotive radar,”, International Conference on Microwave and Millimeter Wave Technology, 2019.

[21] T. Deckmyn, A. C. F. Reniers, A. B. Smolders, H. Rogier, D. V. Ginste, S. Agnessens, "Wideband substrate integrated waveguide antenna for next generation mmWave wireless systems,", *Twelfth European Conference on Antennas and Propagation,* UK, 2018.

[22] Q. Yang, S. Gao, Q. Luo, L. Wen, Y. L. Ban, X. X. Yang, X. Ren, J. Wu, "Cavity-backed slot-coupled patch antenna array with dual slant polarization for millimeter-wave base station applications." *IEEE Transactions on Antennas and Propagation,* vol. 69, no. 3, pp. 1404 – 1413, 2021.

[23] H. S. Huang, C. Y. Ho, C. C. Chu, S. C. Hsieh, C. C. Wang, "Analysis and optimization of a multilayer organic substrate for mmWave antenna in package/module application," *Sixteenth International Microsystems, Packaging, Assembly and Circuits Technology Conference,* 2021.

[24] P. A. Dzagbletey, Y. B. Jung, "Stacked microstrip linear array for millimeter-wave 5G baseband communication." *IEEE Antennas and Wireless Propagation Letters*, vol.17, no. 5, pp. 780 – 783, 2018.

[25] A. K. Pandey, "Phased array antenna with beamforming network for 5G mmWave communication system," *Fiftieth European Microwave Conference,* 2021.

[26] V. K. Kukkala, J. Tunnell, S. Pasricha, T. Bradley, "Advanced driver-assistance systems: a path toward autonomous vehicles.", *IEEE Consumer Electronics Magazine,* vol. 7, no. 5, pp. 18 – 25, 2018.

[27] R. Ferguson, M. Chevrier, A. Rankin, "mmWave radar: enabling greater intelligent autonomy at the edge.", *Future of mmWave Magazine,* Texas Instruments, 2018.

[28] D. M. Grimes, T. O. Jones, "Automotive radar: a brief review.", *Proceedings of the IEEE,* vol. 62, no. 6, pp. 804-822, 1974.

[29] K. Ramasubramanian, K. Ramaiah, "Moving from legacy 24 GHz to state-of-the-art 77 GHz radar.", *ATZelectronics worldwide,* vol. 13, pp. 46-49, 2018.

[30] F. Kolak, C. Eswarappa, "A low profile 77 GHz three beam antenna for automotive radar," *IEEE MTT-S International Microwave Symposium Digest,* USA, 2001.

[31] S. H. Mousavi, A. Porzadi, M. R. Nezhad-Ahmadi, S. Safavi-Naeini, "Wideband corporate center-fed antenna for 79 GHz automotive radar application,", IEEE 19th

International Symposium on Antenna Technology and Applied Electromagnetics, Canada, 2021.

[32] A. Hassanien, W. Swelam, M. H. A. E. Azeem, "16x8 wideband microstrip planar array antenna for E-band millimeter-wave 5G high speed WLAN and broadband internet applications*", IEEE International Symposium on Antennas and Propagation & USNC/URSI National Radio Science Meeting*, USA, 2017.

[33] V. Miraftab, W. Zhai, M. Repeta, "A wideband low-cost E-band SIW antenna array for high capacity mmWave radio,", *IEEE MTT-S International Microwave Symposium*, USA, 2015.

[34] J. H. Lee, J. M. Lee, K. C. Hwang, "Series feeding rectangular microstrip patch array antenna for 77 GHz automotive radar,", *International Symposium on Antennas and Propagation*, 2017.

[35] H. Yao, H. Kumar, T. Ei, N. Ashrafi, S. Ashrafi, D. L. MacFarlane, R. Henderson, "Patch antenna array for the generation of millimeter-wave Hermite-Gaussian beams.", *IEEE Antennas and Wireless Propagation Letters*, vol. 15, pp. 1947 – 1950, 2016.

[36] M. H. Nemati, I. Tekin, "A 77 GHz on-chip microstrip patch antenna with suppressed surface wave using EBG substrate,", *IEEE Antennas and Propagation Society International Symposium*, USA, 2013.

[37] M. Seyyedesfahlan, I. Tekin, "ACP probe measurement of on-chip strip dipole antennas at W-band." *IEEE Transactions on Antennas and Propagation*, vol. 64, no. 4, pp. 1270 – 1278, 2016.

[38] M. Seyyedesfahlan, E. Öztürk, M. Kaynak, I Tekin, "77 GHz four-element phased-array radar receiver front end*", IEEE Transactions on Components, Packaging and Manufacturing Technology*, vol. 6, no. 8, pp. 1162 – 1173, 2016.

[39] O. F. Khan, Multilayer Antenna Design for Automotive Radar at 77 GHz, PhD Thesis, Universität Ulm, 2020.

[40] A. Kuriyama, H. Nagaishi, H. Kuroda, K. Takano, "A high efficiency antenna with horn and lens for 77 GHz automotive long-range radar,", *46th European Microwave Conference*, UK, 2016.

[41] H. B. Ma, J. D. Zhang, X. Y. Chen, W. Wu, "Design of E-band zoned-lens horn antenna,", *IEEE MTT-S International Microwave Biomedical Conference*, 2019.

[42] K. Fan, Z. C. Hao, Q. Yuan, G. Q. Luo, W. Hong, "A wideband high-gain planar integrated antenna array for E-band backhaul applications*." IEEE Transactions on Antennas and Propagation*, vol. 68, no. 3, pp. 2138-2147, 2020.

[43] G. P. Gauthier, N. Dib, L. P. Katehi, G. M. Rebeiz, "77 GHz dual-polarized microstrip antennas on thin dielectric membranes," *IEEE Antennas and Propagation Society International Symposium 1997 Digest*, Canada, 1997.

[44] G. Shen, W. Che, "Compact Ku-band LTCC bandpass filter using folded dual-composite right- and left-handed resonators." *Electronic Letters*, vol. 56, no. 1, pp. 17-19, 2020.

[45] D. M. Pozar, *Microwave Engineering*. John Wiley and Sons, 2012.

[46] G. N. Phung, U. Arz, "Parasitic probe effects in measurements of coplanar waveguieds with narrow ground width," *IEEE 24th Workshop on Signal and Power Integrity (SPI)*, pp. 1-4, 2020.

[47] M. Spirito, U. Arz, G. N. Phung, F. J. Schhmückle, W. Heinrich, R. Lozar, Guidelines for the design of calibration substrates, including the suppression of parasitic modes for frequencies up to and including 325 GHz: EMPIR 14IND02 - PlanarCal, 2018.

[48] X. Shang, N. Ridler, J. Ding, M. Geen, Introductory Guide to Making Planar S-parameter Measurements at Millimetre-wave Wavelengths: EMPIR 19SIP02 PlanarMeT, 2021.

[49] B. Amado-Rey, A. Tessmann, Y. Campos-Roca, H. Massler, A. Leuther, O. Ambacher, "Spurious Mode Suppression in the Design of GCPW Submillimeter-wave Power Amplifiers," *48th European Microwave Conference*, pp. 851-854, 2018.

[50] Singh, F. L. Lohar, B. S. Sohi, "Design of Circular Polarized Patch Antenna for NaviC Receiver Applications." *IOP Conference Series Materials Science and Engineering*, vol.1, 2020.

[51] W. L. Stutzman and G. A. Theile, *Antenna Theory and Design*. John Wiley and Sons, Inc., 1998.